

Tensile Test Design to Measure Interlayer Adhesion in Investment Casting Shells for Spalling Mitigation

A Senior Project
Presented to
The Materials Engineering Department
California Polytechnic State University, San Luis Obispo

By
Shelby Boyd, Alex Miller, Jameson Senger

Advisor: Prof. Blair London
Industry Contact: Noah Hansen
PCC Structural, Inc.

June 2015

Abstract

We designed a tensile test fixture for a 112 lb_f capacity Instron load frame that imparts a normal force on the face of a button epoxied to an investment casting shell sample, delaminating the shell area attached to the button. Using a green standard shell (Group 1), a partially fired standard shell (Group 2), and a green shell with a different third coat (Group 3), we verified that the fixture can measure differences in strength between sample groups. We attached steel buttons to leveled samples with 0.05 mL of Hysol-Loctite 9340 epoxy, let it cure for 48 hours, and tested them at 0.05 in./min. Most shells failed below the face coat, instead of spalling. Groups 1 and 2 failed in a backup layer, or at the larger stucco beneath it (0.035-0.044" deep). Group 3 failed in the face coat (0.010"), flat in a backup layer (0.033"), or in rounded craters through several layers (0.064"). We measured fracture areas in Photoshop to calculate failure stresses, which averaged 116.21 psi for Group 1, 179.42 psi for Group 2, and 141.99 psi for Group 3, with respective standard deviations of 21.78 psi, 30.84 psi, and 31.21 psi. Two-sample t-tests showed statistically valid distinctions between each group's results, indicating that this fixture could be used to further investigate designing a stronger shell to mitigate face coat spalling.

Keywords

Investment casting, Spalling, Fixture design, Ceramic mold, Slurry, Zircon, Mechanical test, Failure modes, Face coat, Interlayer adhesion

Table of Contents

Abstract	i
List of Figures.....	iii
List of Tables.....	iv
Acknowledgements	v
I. Introduction	1
A. Project Definition	1
1. Problem Statement.....	1
2. Sponsor.....	1
B. Industry	4
1. Investment Casting: History	4
2. Investment Casting: Process Overview	5
3. Investment Casting: Alloys.....	10
C. Mold System.....	12
1. Mold: Manufacturing	12
2. Mold: Refractories	12
3. Mold: Binders.....	13
D. Spalling	16
1. Spalling: Phenomenon	16
2. Spalling: Prevention by Test Design	18
II. Safety	22
III. Test Design	22
A. Testing Fixture	22
B. Epoxy	29
C. Sample Preparation Procedure Development	31
1. Determining Epoxy Volume and Application Method.....	31
2. Tape Test.....	39
3. Photoshop Measurement.....	39
D. Fixture Validation Design of Experiment.....	42
E. Final Procedure	43
IV. Shell Comparison.....	44
A. Testing.....	44
B. Results	46
1. Failure Modes	46
2. Pre-existing Surface Cracks Visual Results	50
3. Testing for Results by Group.....	51
C. Analysis	53
1. Depths	53
2. Surface Cracks	54

3. Difference by Groups	54
4. Materials Mechanisms	55
V. Conclusions and Recommendations	57
Conclusions	57
Recommendations	57
VI. Bibliography	58
A. General Information	58
B. References Cited in Text	58
Appendix A: Sample Surfaces Before Testing	61
Appendix B: Button Surfaces After Testing	67
Appendix C: Depth Results and Statistics	73
Appendix D: Surface Specks Graph	78
Appendix E: Statistical Analysis of Groups	78

List of Figures

Figure 1. PCC Product Sales by Industry	2
Figure 2. PCC’s Sales by Production Technology	2
Figure 3. PCC’s Income Spent on Operating Costs	3
Figure 4. An early copper casting.....	4
Figure 5. An intricate Aluminum casting	5
Figure 6. Die for molding wax patterns.....	6
Figure 7. Diagram of the central sprue	6
Figure 8. Slurry and stucco application	7
Figure 9. Diagram of wax removal.....	8
Figure 10. Pouring of an alloy into a mold.....	9
Figure 11. Modern applications of cast parts	10
Figure 12. SEM pictures of fibers within a Mold.....	15
Figure 13. The influence of slurry pH on slurry gel time	15
Figure 14. Defects from spalling in a cast part.....	16
Figure 15. Fluorescent highlighting of defected region	18
Figure 16. The fixture for ASTM D897	19
Figure 17. Fixture by Ransom & Randolph	20
Figure 18. Button component from Ransom & Randolph.....	20
Figure 19. Spalling load data from the Ransom & Randolph Study	21
Figure 20. First Ransom & Randolph fixture redesign	23
Figure 21. First fixture iteration full assembly	24
Figure 22. The second iteration	25
Figure 23. Final fixture iteration assembly schematic.....	26
Figure 24. Fixture hook and button CAD models	27
Figure 26. Rapid-prototyped gluing fixture.....	29
Figure 27. Machined aluminum gluing fixture parts	30

Figure 28. The assembled aluminum fixture	31
Figure 29. First button and epoxy trials.....	32
Figure 30. Bonding areas from first epoxy trials	32
Figure 31. Initial ceramic and epoxy test	34
Figure 32. Epoxy overflow vs. proper volume application	35
Figure 33. Modified epoxy volumes and leveling	36
Figure 34. Leveled epoxy samples on backing.....	37
Figure 35. Tested samples from epoxy variations	37
Figure 36. Failure stress plot for epoxy variations	38
Figure 37. Attempted foam tape test run	39
Figure 38. Process of scale modification in Photoshop.....	40
Figure 39. Calibration of the scale in Photoshop.....	41
Figure 40. Area measurement in Photoshop.....	42
Figure 41. Steps of sample preparation	43
Figure 42. Leveled glass table with fully prepared samples.....	44
Figure 43. Pictures of surface cracks	45
Figure 44. The expected "typical" spalling failure	46
Figure 45. Quantitative depths of seven visual failure types.....	48
Figure 46. Average stresses of failure modes	49
Figure 47. An interval plot of stress by failure modes	50
Figure 48. Equal variance test for groups' stresses.....	52
Figure 49. Interval plot of the group's stresses	53
Figure 50. How bonds silica particles strengthen green shells.....	55
Figure 51. Diagram of the fired shell	56
Figure 52. Diagram of shell system with the additional third layer	56
Figure 53. Flat and middle failure stresses in Group A.....	73
Figure 54. Flat and middle failure stresses in Group B.....	73
Figure 55. Blue, deep, and middle failure stresses in Group C	74
Figure 56. Test for equal variances in Groups A-C.....	74
Figure 57. Normality test for standardized residuals of stresses by failure mode.....	75
Figure 58. Failure stresses by amount of specks on each sample's surface.....	78
Figure 59. A normality plot of the ANOVA residuals for the groups.....	78

List of Tables

Table I. Epoxy Application Variations and Bond Completeness	33
Table II. Maximum Loads from Initial Pull-Off Tests.....	35
Table III. Details on Failure Modes.	47
Table IV. Tukey Groupings for Stresses by Failure Mode.....	49
Table V. Effect of Pre-Testing Surface Cracks on Failures.	51
Table VI. ANOVA Results for Failure Stresses by Sample Group.....	52
Table VII. Pre-Test Surface Comments	61
Table VIII. Button Surfaces from Preliminary Testing Groups B-D.....	67
Table IX. Button Surfaces from Groups A-C, Final Tests	68

Acknowledgements

We would like to thank Noah Hansen and Dr. Jack Hyzak from PCC Structural, Prof. Blair London from the Cal Poly Materials Engineering Department, and Prof. Heather Smith from the Cal Poly Statistics Department, as well as the rest of the Materials Engineering Department faculty and staff.

I. Introduction

A. Project Definition

1. Problem Statement

Spalling is a common surface defect in the investment casting industry, where part of the investment shell's face coat falls off and it causes extensive rework and scrap for weldable and no-weld parts. Precision Castparts Corporation (PCC) Structural. San Leandro sees occasional spalling of the zircon face coat in fillet radii of nickel-based superalloy investment castings. The literature on investment casting is clear that spalling is one of the least-understood surface defects in castings. However, overall investment shell strength is understood to depend on the retained moisture, amount of binder and solids, and pH of the shell system. This project will test the assumption that spalling is less likely to occur in a shell with stronger bonding between its first two coats. We will design a repeatable tensile test to quantify this face coat delamination strength as the tensile strength calculated from measured failure loads and fracture surface areas. Failure loads should be less than 100 lbs. Minor variations in the shell structure will help determine the sensitivity of the tensile testing procedure and apparatus. This will lead to recommendations for future steps to identify factors in shell composition that mitigate spalling.

2. Sponsor

Based in Portland, Oregon, PCC has advanced investment casting technology since their founding in 1949. At the time, the largest investment castings weighed 3 lbs, but they developed the technology to make 55-lb parts to fulfill a contract with Solar Turbines ["History of PCC"]. PCC Structural, a separate division since 1986, currently casts the largest diameter nickel-based superalloy, titanium, and stainless steel investment castings, making parts up to 100 inches across [PCC Report 1]. PCC is the international industry leader for cast and forged parts used in aircraft engines, airframes, power generation, armaments, medical. With 50 domestic and 6 international investment casting facilities, they are still growing and expanding their capabilities by acquiring aerostructures manufacturerers [PCC Report 6]. Their sales have increased over the last few years, from \$6,208.7 million in fiscal 2011 to \$8,377.8 million in fiscal 2013 [PCC

Report 7]. Figure 1 shows the sales for the major industries PCC serves, while Figure 2 breaks down the processing technology used to meet those needs, and Figure 3 shows the amount of income each processing industry spends on operating costs. The higher percentage of operating income spent on investment casting may be partially unavoidable due to the process's labor- and time-intensive nature. However, spalling currently accounts for 6% of the total scrap, and 3% of the total rework at PCC Structural, San Leandro. If it could be eliminated or even mitigated effectively, it would help reduce operating costs.

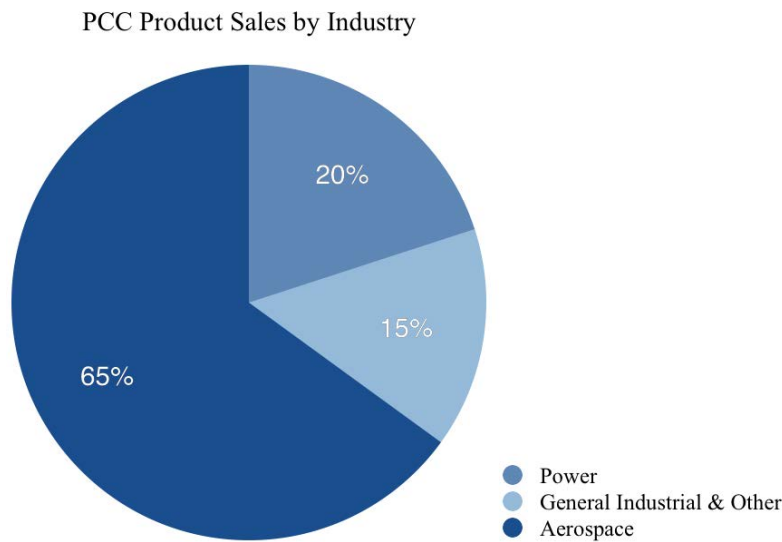


Figure 1. PCC Product Sales by Industry. PCC products are used for power, aerospace, and general industrial needs, as well as some “other”. In fiscal 2013, 65% of PCC’s sales went to the aerospace industry [PCC Report 7].

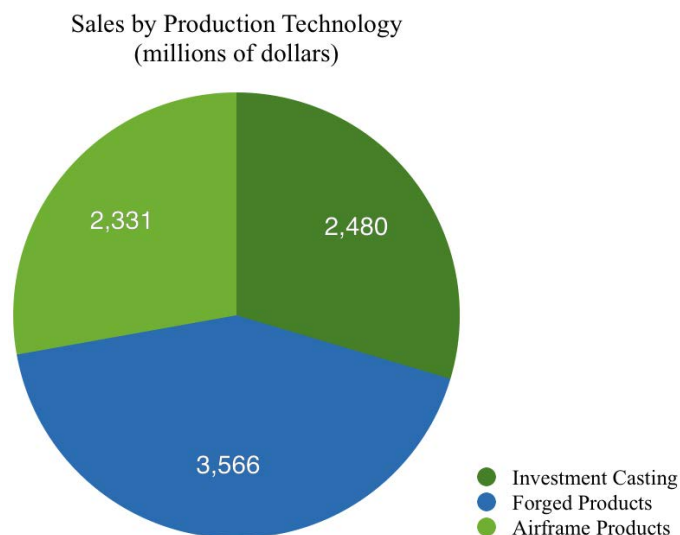


Figure 2. PCC’s Sales by Production Technology. The three technologies PCC focuses on are investment casting, forging, and airframe products. In fiscal 2013, 42.6% of PCC’s sales came from forged products, while 29.6% was from investment castings, and airframe products made up the last 27.8% [PCC Report 29].

Income Spent on Operating Costs
(millions of dollars)

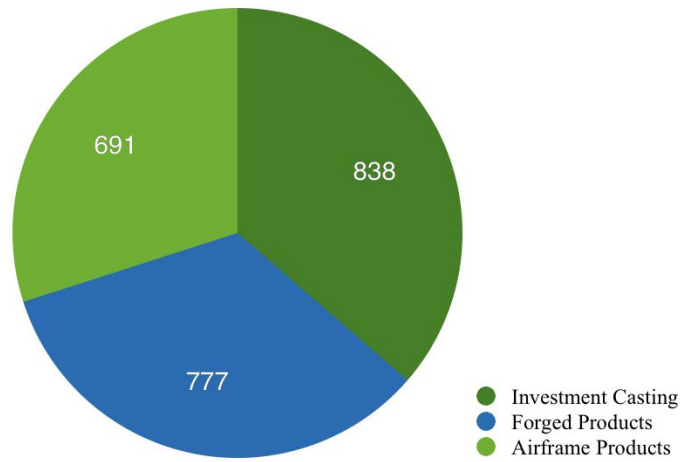


Figure 3. PCC's Income Spent on Operating Costs. Part of PCC's sales from each technology focus is spent on operation costs. In fiscal 2013, investment casting plants spent 33.8% of their sales on operations, while forging plants spent 21.8%, and airframe products spent 29.6% [PCC Report 29].

B. Industry

1. Investment Casting: History

Modern investment casting began as an intricate art, and has developed into a highly technical field. When potters in West Asia discovered smelting between 5000-4000 B.C., they began casting metals from the smelted ores [Jones and Yuan 258. Pattnaik, Karunakar, and Jha 2333. Cramb 1]. The first investment castings were simple copper tools made in open-faced molds, and the process soon developed to use two-sided molds [Hunt 63]. Lost wax, or “cire perdue” investment casting is standard practice today, but was first applied around the fourth millennium BC. This process covered a wax figurine with clay, and then melted the wax out by firing the clay. As potters began making these figurines by pouring molten bronze, gold, and copper into the clay molds, instead of sculpting them from stone or clay, they revolutionized religious practices between 3500 and 3200 BC [Hunt 64]. At first, most pieces made with the lost wax process were artistic. Simple copper and bronze tools could be sandcast, but the more detailed features on artwork were better suited to investment casting (Fig. 4). Beeswax was common, and the lost wax process spread easily as art traders brought castings to new regions. Starting in Mesopotamia around 2800 BC, lost wax casting was a common practice in Greece and the surrounding areas by 2500 BC [Hunt 65]. Eventually, civilizations across the world were investment casting, from the Indus Valley to the Aztecs and Incas.



Figure 4. An early copper casting of a Sumerian king in a chariot, dated around 2850 BC [Hunt 64].

While the lost wax process allowed artists to make increasingly intricate pieces, it did not become a technical field until the Second World War, when advanced machinery required components with complex geometries and properties too difficult to achieve with traditional

metalworking methods. Following the war, the industry continued expanding because of its ability to produce a wide range of parts with complex shapes, smooth surfaces, and high tolerances (Fig. 5) [Pattnaik, Karunakar, Jha 2333]. Investment casting is now a large technical field, as shell-forming methods have improved and industries require increasingly large monolithic components. Some typical parts requiring an investment casting process are gas turbine blades, cogwheels, implants, and nuclear reactor components [Jones and Yuan, 258].

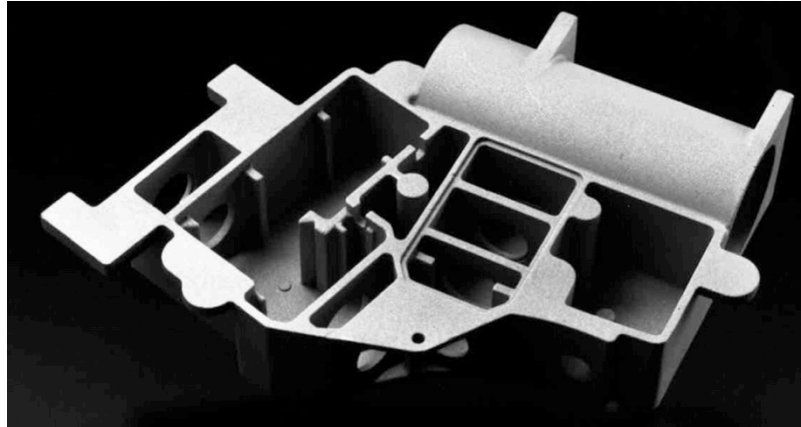


Figure 5. An intricate Aluminum casting (Aluminum 356). This casting from AlCuMet, Inc. shows some of the thin walls and intricate sections possible in investment cast parts [“Casting Capabilities”].

2. Investment Casting: Process Overview

The investment casting process begins with a wax pattern in the shape of the final part. Dimensions of this pattern are modified from those of the final part, accounting for the difference in the wax and metal's thermal expansion coefficients and the cast alloy's solidification shrinkage. Traditional pattern materials include beeswax, carnauba wax, polystyrene, and resins. Modern pattern materials include carnauba, paraffin, amide, and ester amide waxes. Synthetic waxes are common in the investment casting industry due to their customizability; variations in working and blending procedures can produce a range of melting points between 35 and 200°C and freezing shrinkage as low as 3% [Bidwell 22-25]. For smaller parts, several patterns are grouped together and connected to a vertical sprue by a series of horizontal gates. Wax is cast in a die to emulate the desired shape and tolerances of the part and connective gates (Fig. 6). Die components can be manufactured from metals, resins, or elastomers, but the more complex and high-tolerance dies are typically machined from aluminum or steel alloys.

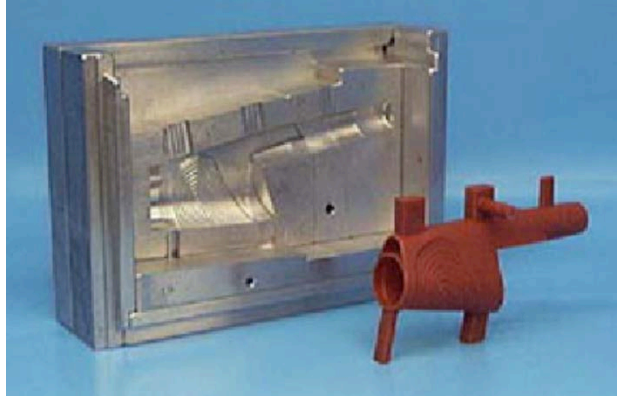


Figure 6. Die for molding wax patterns. This is half of a die used to cast wax patterns. The hollow in the wax pattern is formed by a dissolvable ceramic core [Alcoa].

Patterns are made with virgin wax, but the remainder of the gating system can be constructed using reclaimed pattern wax. The gate sections of the patterns are melted with a heated spatula and pressed against the sprue pattern, where they cool until the interface solidifies. The result is a ‘tree’ of wax patterns attached radially to the central sprue (Fig. 7).

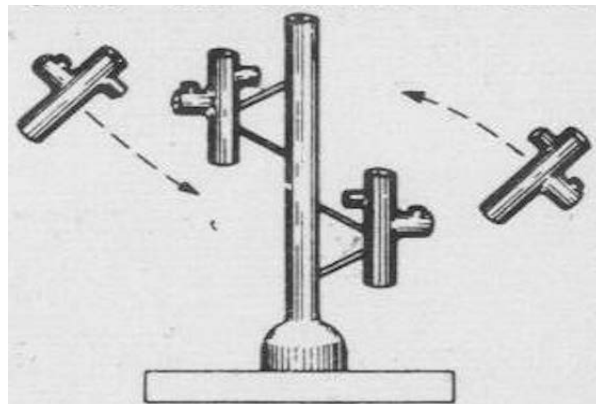


Figure 7. Diagram of the central sprue. Wax patterns are attached radially to the central sprue, allowing multiple parts to be cast from a single shell mold [Diamond 289].

The molds produced from the wax patterns are made monolithically by applying a series of refractory ceramic coats to the surface of the pattern assemblies (Fig. 8a). Refractories are defined as “nonmetallic materials having those chemical and physical properties that make them applicable for structures, or as components of systems, that are exposed to environments above 538°C (1000°F)” [ASTM C71]. The pattern assembly is dipped in a continuously mixed and regulated slurry bath, typically composed of a water-silica binder and a zircon particle "flour". After dipping and allowing excess slurry to drain off, the surface is stuccoed with zircon sand with either a rainfall or fluidized bed system (Fig. 8b). The second slurry coat may use the same

slurry, or one with an adjusted refractory content depending on the desired mold properties. After the slurry supporting each stucco coat has dried, additional coats of slurry and stucco are applied until the mold wall reaches a sufficient thickness. This measurement varies by supplier, but the range of thicknesses between the inner and outer walls is 6-10 mm. After the last coat has dried, the mold can hold its shape but has not formed ceramic bonds between the applied coats. Once a full mold has been assembled in this ‘green’ state, the pattern wax is removed from the shell.



Figure 8. Slurry and stucco application **a)** The first and second slurry and refractory coats are applied to wax pattern trees by hand to ensure all surfaces are coated. The backup coats are applied robotically. **b)** A rainfall system is one of two stuccoing methods used to cover the new slurry coats with refractory particles before they are dried [Process, AlCuMet, Inc.].

The wax removal procedure typically takes place in an autoclave heated with saturated steam (Fig. 9), which liquefies the wax at the mold interface so it can drain before it has a chance to expand and strain the shell. The vessel is pressurized at 550 to 620 kPa in 4-7 seconds, liquefying the wax in 15 minutes or less. The liquid wax is drained and around 75% is reclaimed for later use [Horton 652]. Less common methods include flash dewaxing, in which pressure is not applied and wax combustion is more likely; and liquid dewaxing, in which a heated liquid melts the wax. Pattern removal leaves a partially fired and mostly empty ceramic investment mold.

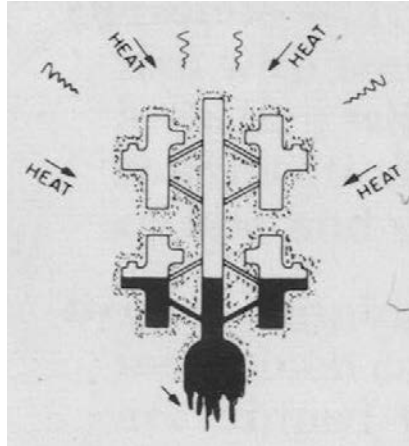


Figure 9. Diagram of wax removal. Wax is removed from the green shell by applying heat and letting the wax run out of the mold. Any remaining wax is burned out in a subsequent step [Diamond 289].

In the green state, the molds contain water, organic compounds, and pattern wax. These are removed by firing the molds between 870 and 1095°C [Horton 653]. Heating rates for the mold can vary depending on the slurry compositions, but because of the investment shell's thin walls, the firing time is generally on the order of several hours [Diamond 289]. At the operational temperature, 10% excess air is provided to ensure the full combustion of residual organic compounds. The firing causes chemical reactions in the shell to form structural bonds between layers, giving the mold the strength to support the molten metal later in the process. The solid mold is ready for casting after firing burns out excess materials and sinters the layers and particles together.

Arc, induction, and vacuum furnaces are used to melt the alloy before casting. The investment molds are preheated to high temperatures, reducing thermal shock to the ceramic material from the pouring of the melt. For steel and superalloys, molds are typically preheated to between 870 and 1095°C (Fig. 10). Some casting methods affix the mold to the mouth of the furnace and rotate the assembly 180°, filling the mold while minimizing turbulence in the melt. Other methods simply use gravity to fill molds held in a vacuum, or centripetal forces in rapidly rotating molds to distribute the melt across vertically oriented features inside the mold walls. Regardless of the casting method, the mold and casting must be allowed to cool and solidify before proceeding to the break out stage.



Figure 10. Pouring of an alloy into a mold. Some alloys can be poured into the mold in a standard atmosphere [Process, AlCuMet, Inc].

The bulk of the ceramic shell is removed using vibratory hammers, typically in spaces that can absorb sound and manage large amounts of dust. This stage removes the outer layers of the shell, but the primary layer typically adheres more tightly to the surface of the metal and must be removed separately. This can be accomplished mechanically by shot or vapor blasting; or chemically dissolving the remaining refractory layers. Shot blasting is widely used for most castings, but chemical dissolution methods can be required for more complex geometries or parts that have a risk of deforming. Full shell removal leaves the cast metal part exposed, but with a number of extra metal regions from the gating system still attached.

To clean and prepare the parts for shipment, they are passed to the cut-off department. Runners and unwanted features are usually removed from steel and superalloy castings using an abrasive wheel with a rotational speed of 3500 rpm [Horton 655]. Other abrasive wheels, belts, or hand grinders can also be used to further refine the finish of particular regions of the castings. Depending on the tolerances associated with the part in question, additional quality checks may be used to ensure that dimensions and mechanical properties fall within acceptable bounds. Parts are analyzed radiographically and ultrasonically to detect unwanted material inclusions or mechanical defects. If no defects or errors are found in the final cast product, it is ready for shipment.

3. Investment Casting: Alloys

Although investment casting takes is a lengthy, labor-intensive process, it is the only process capable of making such detailed and complex parts from highly alloyed metallic systems. While each alloy system used in investment casting has particular properties and applications, most have can withstand extreme thermal, mechanical, and chemical environments. They are workable enough for final fabrication to produce quality parts, and have good fluidity and feedability. For this reason, the additional labor cost balances with operating savings, making the process cost-effective.

While most standard investment cast alloys can be melted and cast in air, some oxidize too quickly and must be processed in a vacuum, which improves the purity and properties of the final product. These more reactive metals include γ' Ni-base superalloys, some cobalt alloys, titanium, and refractory metals; while steels, ductile iron, magnesium, copper, aluminum, and other cobalt alloys can be air-cast [Horton 654]. Vacuum melting and casting are becoming more standard with the increasing demand for superalloy parts. Common investment cast parts include gas turbine blades, structural castings for nuclear power plants, airplane frames, and surgical implants (Fig. 11).

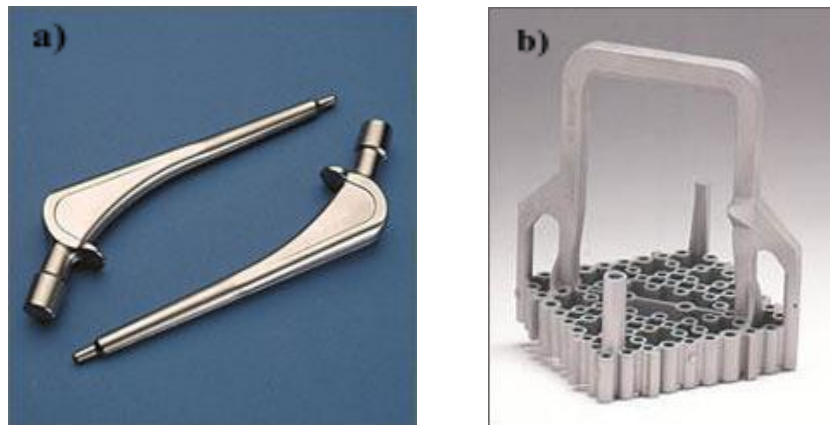


Figure 11. Modern applications of cast parts **a)** Hip implants and **b)** uranium rod holders for nuclear power plants are two well-known investment-cast parts [PCC Structurals].

Developing jet engine technology during WWII required better creep and rupture properties for metal in high temperature and stress environments, which led to the first technical investment castings. Cobalt alloys were first cast for jet engine parts in 1941, and can also be used for cutting tools, dental implants, and surgical implants. In general, cobalt alloys are solid solution strengthened by Cr, W, and Mo, and precipitate strengthened with carbides formed by

0.60-2.5 %C. Castings are finished by machining or grinding depending on the hardness of the alloy [Diamond 221].

In 1954, the US Bureau of Mines used graphite molds for the first titanium alloy castings. Until investment casting titanium became possible in the 1960s, there was no technology that controlled the interactions between the melt and environmental elements tightly enough to make pure titanium castings. Titanium must be vacuum poured because it oxidizes quickly, and is generally hot isostatic pressed (HIPed) after solidification to close voids. The most common alloy is Ti-6Al-4V, which is HIPed at 900°C under 103 MPa for 2 hours. As casting technology has improved, titanium products have evolved from structural panels to medical implants and jet engine components [Granta. Cotton, Clark, and Phelps 1-2].

Nickel-based superalloys are celebrated for their insusceptibility to corrosive environments and temperature-resistant mechanical properties up to 1200°C [Granta]. Only some tungsten and cobalt alloys have higher service temperatures. Coherent γ' precipitates in an austenitic FCC matrix strengthen nickel-based alloys, and remain stable with excellent mechanical properties at these high temperatures. Combinations of Cr, Co, Mo, W, Re, Ta, Hf, Nb, Ti, Al, Zr, C, and B form carbides and a solid solution, providing additional strength. The Cr and Al form protective oxides on the metal's surface, which contributes to the high temperature capability of these superalloys [Das 193, 196].

Steels have low service temperatures because the precipitates providing most of their strength will resolutionize or diffuse into a softer form when exposed to moderately high temperatures. Investment cast stainless steel parts can be used in femoral stems for hip replacements, or as the support structure for glass walls. Steels are the cheapest alloy system used for investment casting. For example, AISI 4130 costs \$0.73/kg, while INCONEL 713, a Ni-Cr alloy, costs \$30.3/kg [Granta]. Because of their low cost, steels are structurally optimal for standard temperature and low corrosivity environments. Chromium in stainless steels limits the reactivity final parts by forming a passive oxide layer.

C. Mold System

1. Mold: Manufacturing

As discussed previously, green investment shells are a composite of slurry coats and refractory sand. The slurries usually contain water, binder, refractory flour, a surfactant, an antifoaming agent, and a bactericide. The mold system requires high thermal shock resistance to minimize cracking when filled, high chemical stability to avoid reactions between the mold and metal, high thermal conductivity so the metal can cool with a desirable microstructure, limited creep to maintain dimensions, and sufficient permeability so trapped air can escape. Molds are made by dipping the wax pattern in a slurry system, rotating it to coat all faces, letting it drain, and coating the slurry coat with refractory powder. The powder reduces stresses induced by drying and assists in the bonding between slurry coats [Jones and Yuan 258]. Between each stuccoing and the next slurry coat, molds made with water-based slurry binders are dried until the water evaporates. Drying can take 2-24 hours, and if not dried completely, the current coat will be too weak for the next one to be applied [Jones and Yuan 260].

2. Mold: Refractories

The refractory flour in the slurries can be the same as the refractory powder applied between slurry coats, but this is not always the case. Because the first coat, called the “prime”, “primary”, or “face” coat, interacts with the molten metal and is the contact surface that determines the casting’s final surface texture, this coat uses finer and more inert refractory flour. Refractory particle size, composition, and amount are chosen based on which slurry coat was applied, the system of the active coat, and the alloy system. Some refractory materials react with the binder system during gelling, or with the melt during casting. The backup coats use less expensive and coarser refractories because the larger particles allow more gas to escape as the melt is poured into the mold, reducing gas porosity and improving mechanical properties in the casting [Horton 650. Chen et al. 344].

Refractory materials require high dimensional stability, consistent chemical and physical characteristics, compatibility with a wide range of alloys, availability in correct size distributions, and a reasonable price. The common ceramic refractory flours are silica sand, aluminosilicates, aluminum silicate, zirconium silicate, and zircon. In particular, two popular refractory particles are zircon or aluminosilicate sands. Zirconia is used specifically because it is

both less expensive than other options, and unreactive with many alloy systems, including highly reactive alloys. Aluminosilicates are rather unreactive to most alloy systems and also relatively inexpensive. Both are frequently used as the refractory particles for the primary slurry coat [Jones and Yuan 259. Cheng et al. 3061].

Refractory particles control the final mold strength and porosity by how they stack in the dried layers, which is determined by the slurry viscosity and particle size distribution of the refractory flour [Chen et. al 346]. Investment casting molds generally have at least 30% porosity from spaces in the stacking of slurry components, and the rough surface provided by the refractory powders [Jones, Yuan 263]. Because the mold has a single inlet, the shell must allow gases from the mold and melt-mold interactions to escape, preventing gas porosity in the final casting. A casting's success depends on its mechanical properties, which are significantly lowered by any defects, including gas porosity.

One of the preferred materials for prime coat slurries is zircon ($ZrSiO_4$). Zircon slurries have high melting temperatures, high oxidation resistance, and high wear resistance, all which are ideal properties for casting [Han 239]. Current processing parameters are unable to fabricate this compound in bulk. Upon cooling after sintering, the ceramic experiences a 3-5% volume increase as excess zirconia transitions from a tetragonal to a monoclinic structure, causing bulk materials to destruct. For structural applications, zircon-zirconia refractories must be stabilized by additives such as yttria (Y_2O_3), magnesia (MgO), or calcia (CaO) [DePoorter 1022].

3. Mold: Binders

In addition to gas permeability, successful investment casting molds require a high strength, especially during dewaxing and pouring the melt. Dewaxing occurs before the shell has been fired, when it is still "green", but must have sufficient strength to remain intact during wax removal. Improper dewaxing will destroy the mold because its coefficient of thermal expansion is about 40 times less than that of the pattern wax [Horton 652]. Slurries made with an alcohol-based binder are stronger in the green state than those with a water-based binder. Fibers or polymers added to both systems increase green strength per coat, and make dewaxing easier [Horton 650, Pattnaik, Karunakar, Jha 2338].

Many current binder systems in industry are water-based colloidal silica systems. Suspension systems for the binders can be either water-based systems containing colloidal silica,

or alcohol-based systems containing ethyl silicate. Many foundries used to use ethyl silicate because it dries quickly. However, growing environmental awareness over the past two decades has revealed concerns about the volatile organic compound released by alcohol-based systems [Pattnaik, Karunakar, Jha 2339]. In the UK, The Environmental Protection Act of 1990 phased out the use of alcohol-based systems by 1997, leading to the implementation of water-based systems that have no regulated emissions, but dry much more slowly [Leyland and Smith 34]. Many foundries in the UK and some US states have been forced to make this switch.

The gelling process for water-based systems requires a long dehydration time, while alcohol-based systems can be chemically gelled and have short drying times. Another advantage of alcohol systems is their high refractoriness, which yields similar refractory properties with a lower mass of refractory material. The lower refractory mass leads to higher porosity of the dry shell and smoother surface finishes than water systems. Water-based systems tend to have lower green strengths and are therefore prone to cracking during wax removal, but have higher fired strengths [Pattnaik, Karunakar, Jha 2339]. This green state weakness can be compensated for by adding liquid polymers or organic fibers, which increase the green strength, but burn out after firing (Fig. 12), reducing the fired strength and increasing porosity. Organic fibers and liquid polymers serve the same purpose, but the liquid polymers lose strength when exposed to steam, making organic fibers a better choice for systems using a steam autoclave to dewax [Yuan and Blackburn 1082]. Polymer additives in water-based systems also reduce the “wet back” between coats, or the amount of moisture re-introduced to the dehydrated coats when a new coat is applied [Jones and Yuan 259].

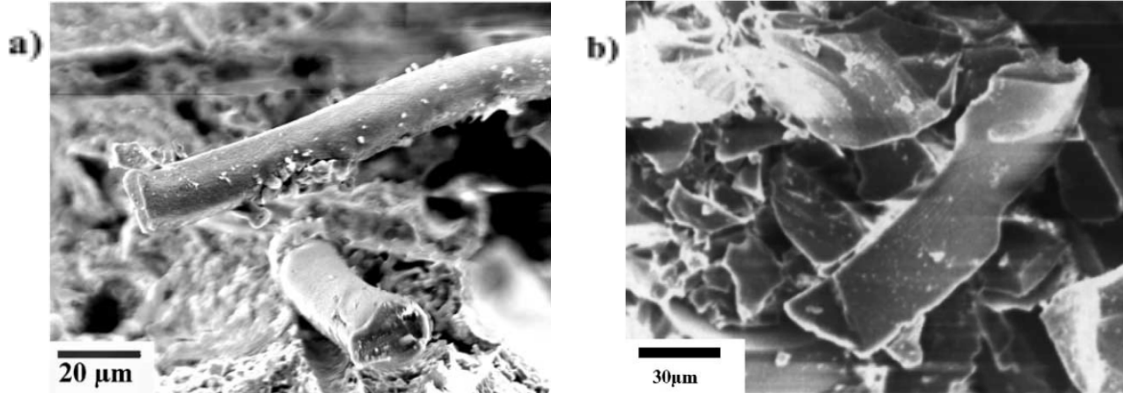


Figure 12. SEM pictures of fibers within a Mold **a)** Nylon fibers in this SEM image of a green shell fracture surface did not break, and provide the mold with higher green strength. **b)** Firing the mold volatilizes the fibers, leaving the voids shown in this SEM image, which increase porosity in the mold by $4 \times 10^{-13} \text{m}^2$ at 800°C [Jones and Yuan 263-264].

A key function to the slurry gelation is its pH. Slurry pH's are regularly checked and corrected. Slurry pH measures the ion concentration within the suspension, where more positive or negative ions respectively lower or raise the pH. With a high ion concentration, particles in the slurry have an increased net charge and repel each other instead of flocculating. Figure 13 shows a graph comparing the log gel line and the pH of slurries. The pH range between 5 and 6 is described as unstable, while the range between 1.5 and 2 is considered stable. Slurry stability is primarily regulated through pH control, but can also be manipulated with dispersant variation [Houivet 610, Bidwell 40].

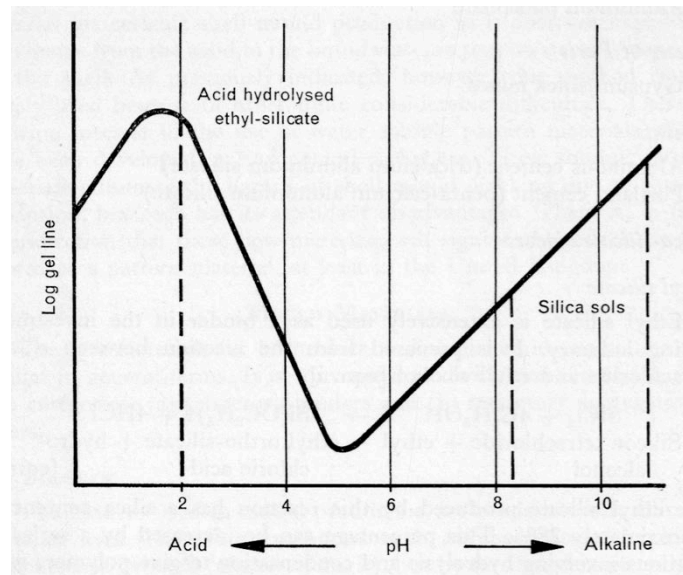


Figure 13. The influence of slurry pH on slurry gel time. The colloidal silica slurries (“silica sols”) gel in a stable manner between pHs of 8-11. Ethyl-silicate slurries gel the most reliably at pH less than 2. Slurries between pH 2-8 are unstable. This graph shows why slurry pH must be maintained to form high quality molds [Bidwell 40].

D. Spalling

1. Spalling: Phenomenon

Surface defects in investment cast parts pose serious problems for parts with high tolerances and limited weldability. One defect, called “spalling” has been observed in processes industry-wide, but no mechanisms have been identified as the root cause. Spalling occurs when part of the prime coat breaks away from the main body of the mold, or “spalls”, leaving an open space on the inner face coat of the mold. The melt fills this space, leaving a raised area on the surface of the final cast product called “plus metal” (Fig. 14). Because part of the mold is detached from the inner shell, porous ceramic inclusions commonly accompany the plus metal and can be observed with fluorescent penetrant marking techniques. A spalled part is most clearly identified by the plus metal on its surface. Theories abound concerning the main contributing factor behind spalling, including specific shell geometries, refractory and binder slurry compositions, excessive porosity as a result of incomplete water removal during burnout, and a general lack of attention to quality control during mold preparation.



Figure 14. Defects from spalling in a cast part. Two spalling defects present on the surface of an investment cast nickel-based superalloy part. Fillet radii are common locations for these defects [PCC Structurals].

Several steps during the mold production process have been identified as possible points of origin for spalling defects. Because ceramic inclusions come directly from the shell, Jackson,

Singh, and Thornton suggest that the slurry dipping steps should be carefully monitored [37]. The slurry coats, particularly for primary layers, should be as uniform as possible to encourage interlaminar bonds of comparable strength in disparate regions of the mold. Careful management of density, pH, and material composition may also contribute to a more uniform mechanical performance across the dipped layers. One of two drying process controls can be implemented, depending on the mold in question. The first allows the prime coat to dry just enough for the colloidal silica to gel sufficiently, leaving water in the coat but cutting down on processing time significantly. The second option allows the prime coat to dry entirely, maximizing the mold's strength against dewaxing damage but regularly increasing processing time by up to 24 hours. Unfortunately, if spalling occurs in this stage, it may not be observable until breakout if the defect is hidden deep within the mold.

The steps following dewaxing may also affect the probability that spalling will occur. The firing and melt pouring steps generally take place at temperatures above 870°C for high-performance structural alloys. Molds composed entirely of silica, or silica with zircon refractory flour, are allotropic, and at this temperature transform into the silica polymorph known as cristobalite. This transformation benefits the casting process because it remains metastable between 270 and 1470°C, allowing the metal to reach its solidus point before the shell begins its next transformation. When the cristobalite cools below 1470°C, it transforms to a hexagonal crystal system and contracts volumetrically, but fast cooling allows the cristobalite to remain metastable down to 270°C [Akhavan]. This simplifies the breakout stage, but the phase transformation introduces variability that may affect the ceramic bond strength. Molds containing alumina have lower high-temperature strength, but are not allotropic. If this strength correlates to the interlaminar strength of the dipped ceramic layers, the lower strength of alumina shells could result in a spalled region in the mold. While both shell types could theoretically spall, research into the spalling mechanisms has yielded inconsistent results.

Less obvious areas experiencing spalling are commonly found by completely submerging the part in a fluorescent penetrant dye. Capillary action absorbs the dye into porous defect regions. After rinsing the part, the defect regions will glow under UV light, providing a clear map of imperfections in the cast part's surface (Fig. 15).

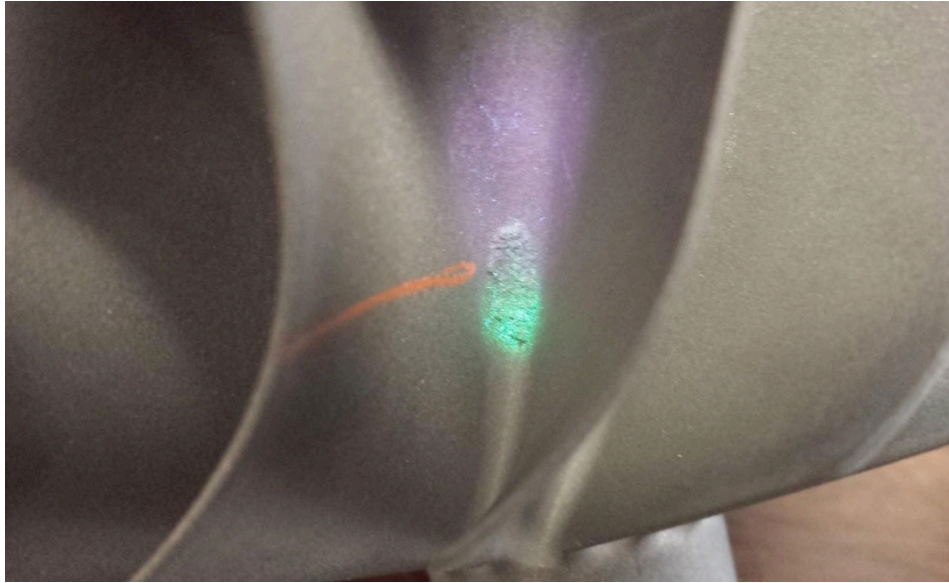


Figure 15. Fluorescent highlighting of defected region .One of the previously shown spalling defects displaying absorbed fluorescent penetrant when exposed to a UV light [PCC Structural].

Regions effected by spalling can sometimes be repaired by grinding off the plus metal. This reveals the affected volume underneath, which must be welded back together to achieve a continuous defect-free surface finish in the right shape. However, many alloys, including structural nickel-based superalloys, are designated ‘non-weldable’ due to the effects of welding on their grain structures. When one of these alloys shows evidence of spalling, the defect is irreparable. If the operative requirements for the part include continuous surface finishes or tightly-constrained grain structures, the part must be scrapped. When large batches of parts do not meet quality specifications in this way, the ramifications for the company are expensive. Mitigating the incidence of spalling is paramount both for overall product quality and for meeting producers’ financial goals.

2. Spalling: Prevention by Test Design

Because spalling occurs when the face coat delaminates from the backup coats, a shell with a stronger bond between these two coats is theoretically less likely to spall. There is no standard test to measure this bond strength, but similar tests exist to measure the flatwise bonding strength of adhesives. One such test uses ASTM D897 to measure the strength of adhesives between two blocks of metal. The fixtures in Figure 16 attach to tensile grips, and the samples places in the center U-shaped slot. This test pulls the samples apart and measures the yield strength of the adhesive as the delamination strength.



Figure 16. The fixture for ASTM D897, holds both ends of a block-adhesive-block assembly in the grips of a tensile-testing machine. The blocks are held in with a collar to even out the force on their top faces [ASTM D897].

A research and development group at Ransom and Randolph developed an adhesion test to measure the delamination strength of investment casting shell face coats [Feffer and Holek]. They evaluated factors involved in spalling by changing composition and processing steps for the shell systems, and delaminated the samples with a tensile test. Ransom and Randolph's first test fixture adhered the straight bolt in Figure 17a to a sample, and pulled it upward through a circular hole in a metal plate Figure 17b. Because the bolt was long and had no alignment mechanism, results from this test varied noticeably if the sample was not completely flat against the bottom of the plate. To improve the test, the bolts were replaced with smaller "T-button", which attached to the crosshead with non-stretch bands (Fig. 18). These bands self-aligned the sample with the plate and crosshead movement.



Figure 17. Fixture by Ransom & Randolph **a)** The initial bolt assembly to which the samples were adhered. **b)** The testing apparatus designed by Ransom and Randolph, with the bonded piece being drawn through a hole a suspended plate [Feffer and Holek 14, 5].

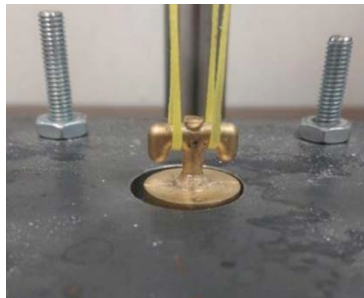


Figure 18. Button component from Ransom & Randolph. A sample (not shown) is pulled against the bottom of the metal plate by the brass T-button, which is connected to the crosshead with yellow non-stretch high load fishing line. The fishing line allows the system to self-align during the test [Feffer and Holek 17].

The Ransom and Randolph study used Hysol Loctite 907 to bond their samples to the button. This two-part epoxy worked well, forming a stronger bond between the face coat and button than existed between the face and backup coats. This test system found the spalling load was between 14-35 lbs (Fig. 19).

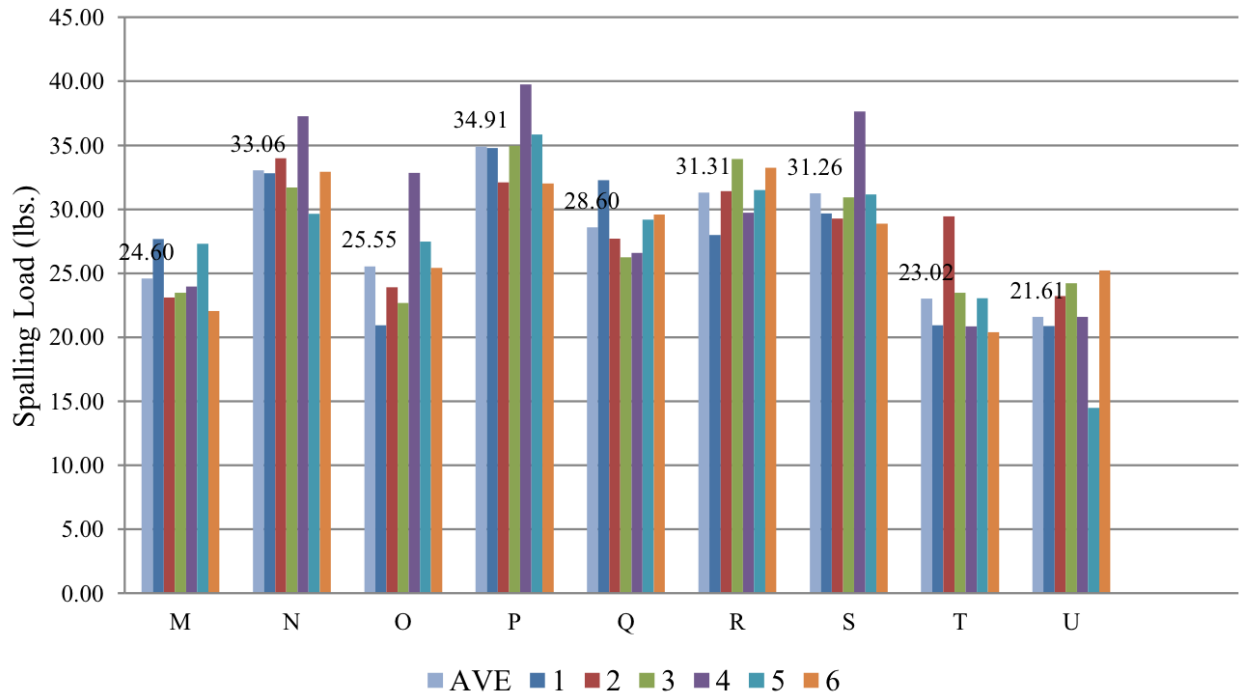


Figure 19. Spalling load data from the Ransom & Randolph Study. Six samples of each shell variation were tested, and their average is the “AVE” bar. While there is a range of data from each shell variation, they group together enough to show a trend based on processing [Feffer and Holek 16].

Ransom and Randolph used their test to show that a shell with higher spalling load is less likely to spall during normal processing. However, their test setup lacks durability and therefore reliability. To continue studying how varying shell composition and processing can mitigate spalling, we developed a similar test, with repeatable procedures for sample preparation, loading, and testing. Because this process includes designing our own fixture, we then tested shell variations from PCC Structurals, San Leandro to determine whether the fixture and procedure can detect differences in strength between systems. In the future, this test will help evaluate the strength of different shells, and hopefully reduce the spalling potential.

II. Safety

We took safety precautions during all stages of this project. We wore eye protection, long pants, and closed-toe shoes at all times while in lab for machining, sample preparation, testing, and epoxy removal. While handling epoxy, we also wore nitrile gloves. When using acetone, we wore a chemical-resistant apron and gloves, and worked in the fume hood. All acetone waste went into the proper disposal container. During testing, samples left ceramic fragments on and around the Instron. Before removing the fixture, we vacuumed these up so they did not fall into and damage the grips.

III. Test Design

A. Testing Fixture

The Ransom & Randolph procedure used a small brass button epoxied to the surface of an investment casting shell section with non-stretch fishing line suspending it from the loading device (Fig. 18). The button protruded through a hole in a plate to apply a load to the adjacent regions of the ceramic coupon. The plate was held in place by four bolts and eight nuts for height adjustment. A tensile load was applied to the button by the non-stretch fishing line until the ceramic's surface fractured at a maximum load. This load was recorded and used to calculate the stress required to fracture the ceramic. While this method applies the desirable loads to the samples, the materials used to construct the fixture are not of a sufficient quality to ensure repeatable results. With these general mechanics in mind, we began development of a more robust construction for the test fixture.

Inspiration for our first design derived from both Ransom & Randolph's test and hardware designated by ASTM D897. This standard uses two slotted cylindrical grips placed face-to-face in a vertical orientation to test adhesive strength between test specimens. Though the standard does not address the strength with which we are concerned, the grip section could be used to test ceramic specimens in a similar way. This component was adapted into the lower half of the prototype fixture design (Fig. 20). We wanted to maintain the flexibility of the fishing line in the upper half of the design while improving the overall strength and reliability of the structure. This goal of consistent orthogonal loading was achieved with a universal ball joint that pinned into the crosshead grip of the Instron Mini 55 testing system. The specific joint used was

a steel ball-and-socket U-joint designated as part number 6441K200 from McMaster-Carr. The combination of the upper and lower components of this fixture provide a more rigid testing frame than the one presented by Ransom & Randolph, while employing the same mechanical principles of even loading and uniaxial stress (Fig. 21). We designed adapter rods to fasten the fixture components to the existing grips in the Mini 55 load frame. All pieces would be held in place with pins of various sizes.

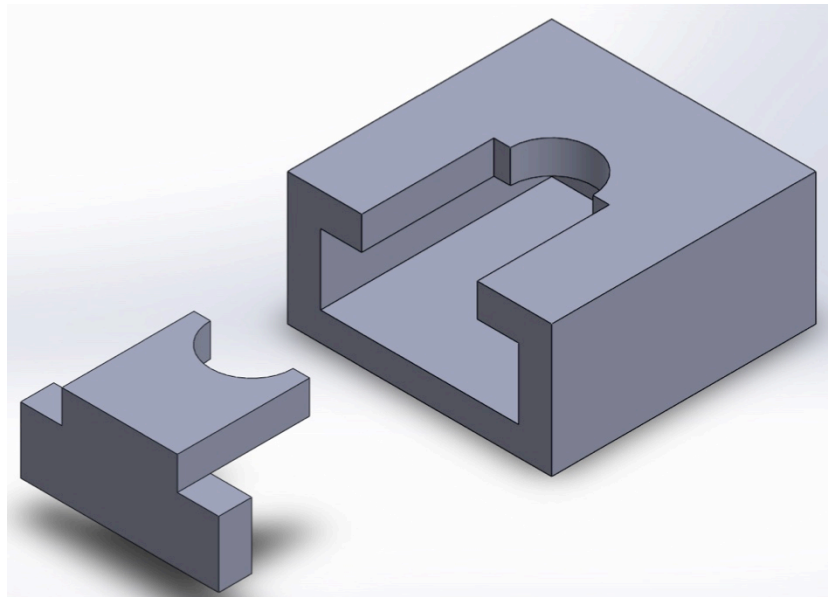


Figure 20. First Ransom & Randolph fixture redesign. The grip modified from ASTM standard D897. This preliminary design was meant to impart even loads on the sample, while remaining easily machineable.

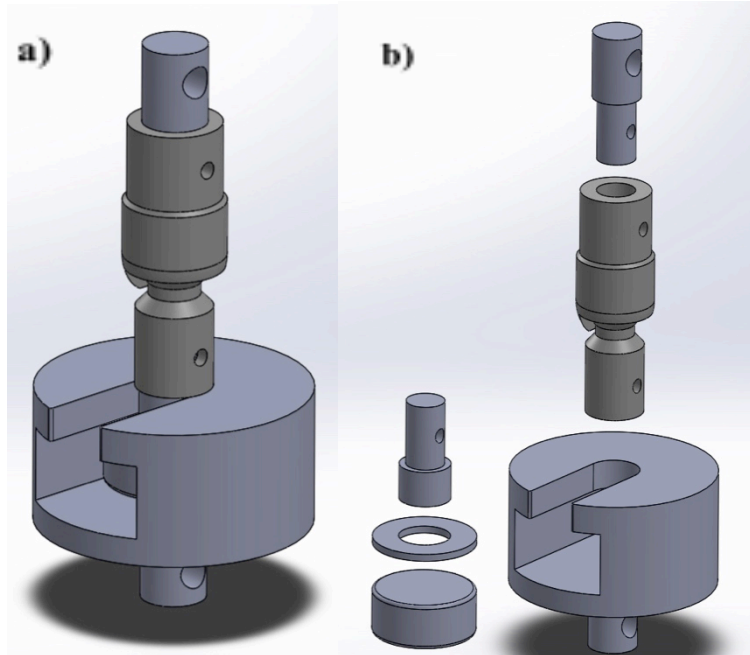


Figure 21. First fixture iteration full assembly **A)** Assembly containing all first-iteration fixture components. **B)** Exploded view of the fixture assembly, with sample setup on left and the fixture setup on the right. The ring provides even loading across the sample given the open slotted section.

Though the first iteration of this design could perform the tests we desired, the geometries of the lower grip component proved too complex for PCC to machine from stainless steel. Machining this component at Wyoming Test Fixtures, Inc. proved a significant financial hurdle to producing more than one fixture. Due to these constraints, the lower half of the fixture required redesign. The result of the redesign efforts was an assembled sample grip that employed a plate-and-rod construction similar to Ransom & Randolph's (Fig. 22). The key difference in this design was the employment of three bolts as opposed to 4, and the plates providing the normal force were circular instead of square. In order to minimize difficulty in mating this grip to the load cell, we opted instead to rely on gravity to suspend it from the crosshead grip. This theoretically eliminated some complex machining otherwise required to sturdily secure the plate to the load cell grip.

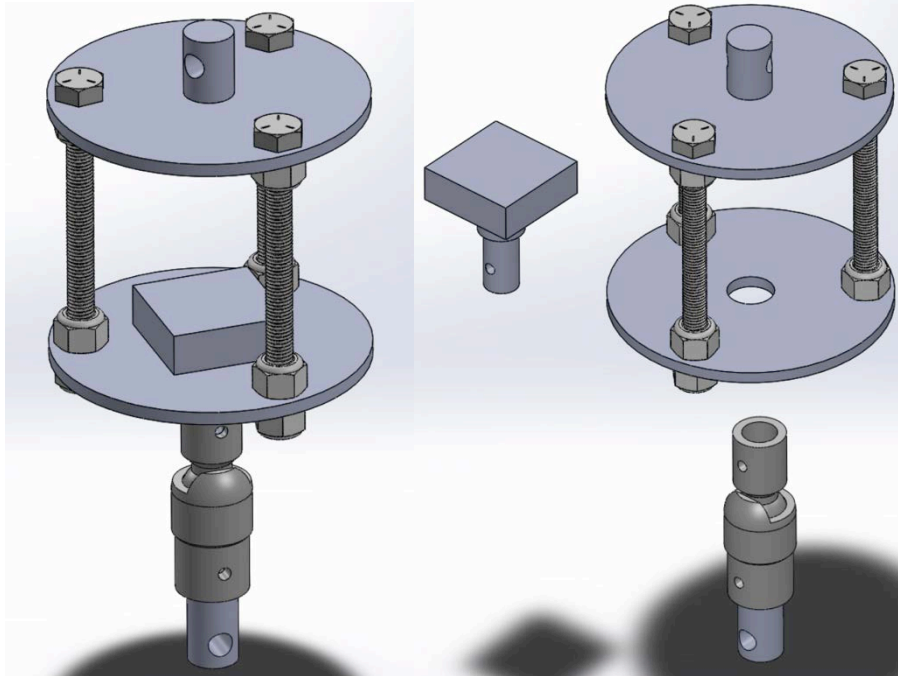


Figure 22. The second iteration (inverted assembly) of our testing fixture. Changes to the sample geometry were taken into account when defining plate and hole dimensions.

The third and final iteration of the testing fixture utilized most of the structural concepts laid out in the second iteration but modified and specialized specific features of the design (Fig. 23). Instead of nuts and bolts, rods with threaded end holes and mated bolts were used to space and support the plates. These rods were chosen to guarantee that the plates remained parallel. We also learned that sturdily securing the bottom plate to the load cell with a threaded rod was within PCC's machining capabilities, so the fixture was reoriented to its original mounting position. This allowed for a redesigned button and upper grip combination that relied on gravity and hinging for load alignment. The button interface portion of the upper grip was changed to a two-pronged hook to support a portion of the button from below. In accordance with this change, the button design changed to keep the sample contact end circular for the purposes of adhesion while introducing a T-stem portion to hang from the hook (Fig. 24). Hanging the button from the hook provided another degree of freedom in which the system could realign itself as test loads gradually ramped up.

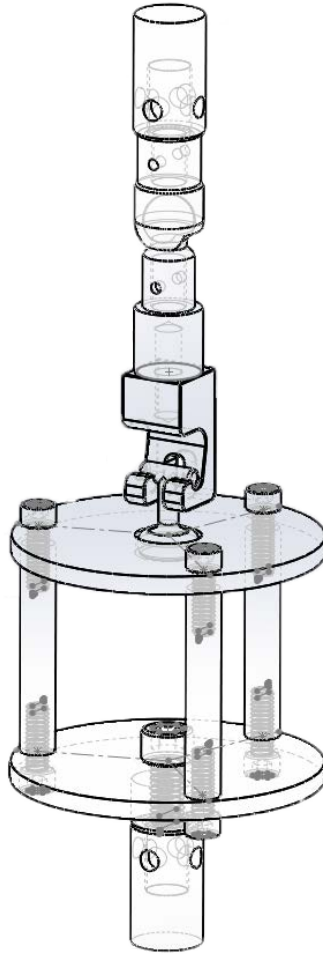


Figure 23. Final fixture iteration assembly schematic. Schematic models of the Instron grips are included for test fitting purposes.

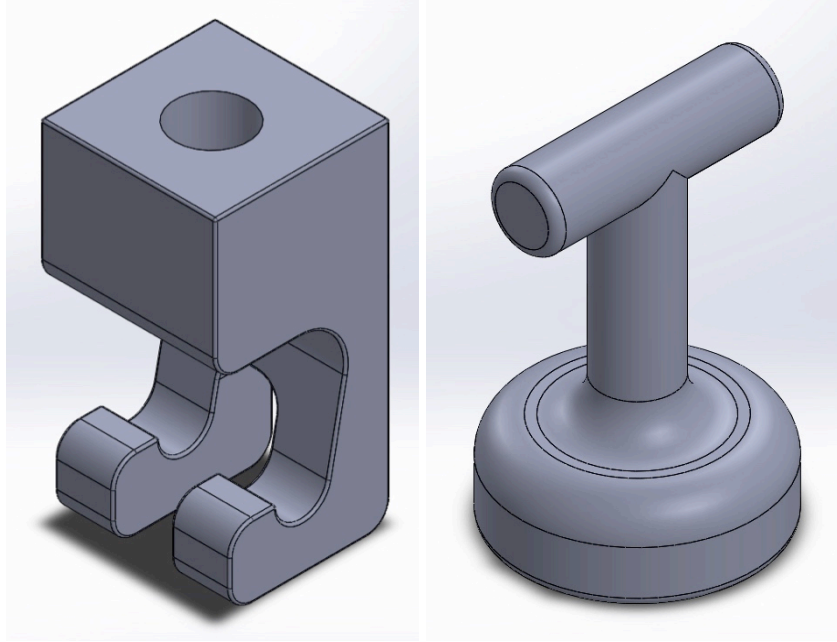


Figure 24. Fixture hook and button CAD models. The hook design for the upper portion of the fixture, next to the button design. The slot between the prongs prevents the button from wiggling while testing. The final button design allows for easy sample loading and realignment during testing.

We sent these modified parts and the unchanged components from the second design iteration to PCC for machining. They investment cast 180 test buttons from stainless steel in order to reduce turnaround time between our tests. After receiving the completed fixture, we checked the fit between the components and the Instron grips. The vertical size in the load frame fell well within the positional limits of the machine (Fig. 25). The adapters fit snugly into their respective grips when pinned in place, giving no potential for misalignment or wiggling during the test. The fit and construction of the fixture met our standards and allowed us to move forward with procedure design.

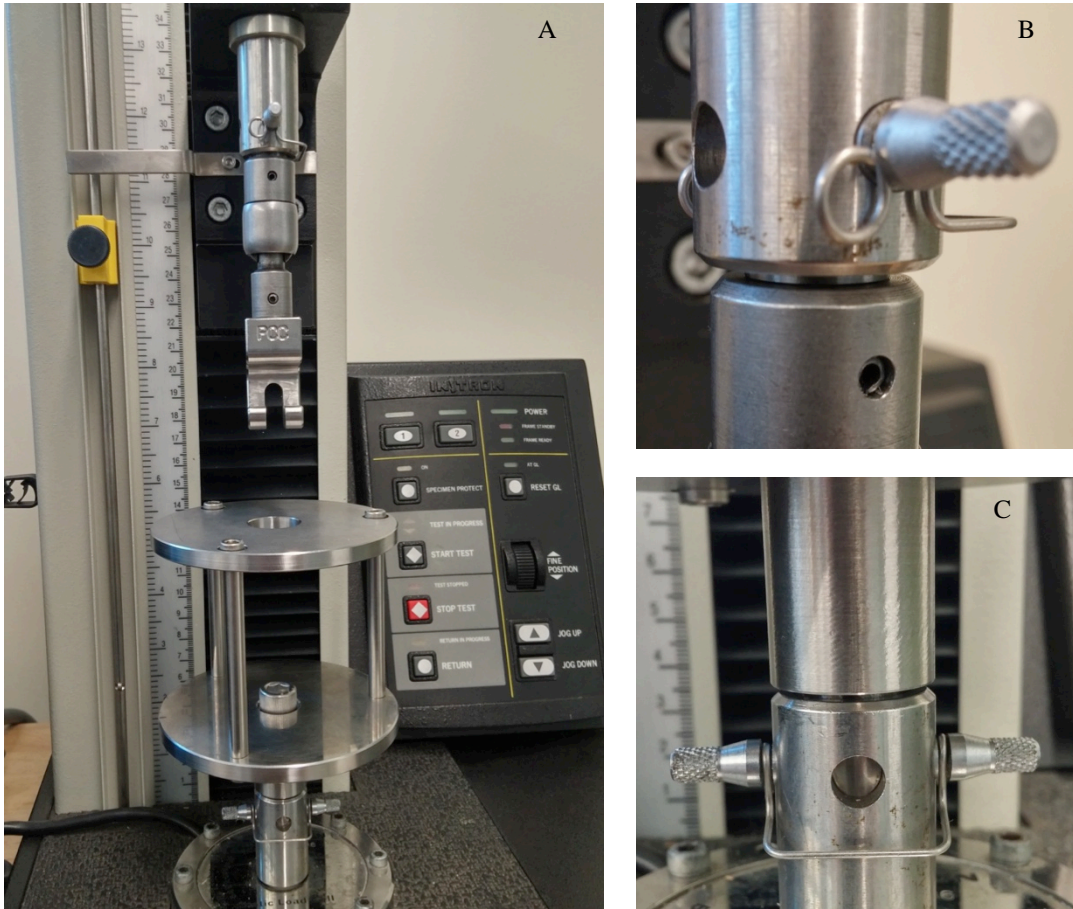


Figure 25. Final machined fixture in Mini 55 machine, displaying its vertical spacing (A), upper adapter pin fit (B), and lower adapter pin fit (C).

B. Epoxy

In order to perform tensile tests on the ceramic samples themselves, we had to select an adequate epoxy to attach the test buttons. We investigated industrial-grade epoxies with high tensile strengths suited for bonding stainless steel to zircon-based ceramics. This research resulted in the selection of Hysol Loctite 9340 Chemical Resistant Epoxy ("Adhesive in a Tube") due to its claimed suitability for bonding both metals and ceramics. The epoxy unit contained a combined total 2.7 ounces of resin and hardener in separate tubes. Calculations of theoretical epoxy volumes per sample told us that this volume would be more than sufficient for the anticipated number of samples to be prepared. After mixing in a 1:1 ratio, the epoxy remains workable for 90 minutes before beginning to harden, providing us with enough time to prepare relatively large sample groups in single batches. Full strength is attained after 72 hours of curing, so the down time between sample preparation and testing is relatively low. These properties met our criteria for a workable structural epoxy, so we purchased one unit.

Prior to receiving the test buttons and epoxy, we began developing a method for applying epoxy to the buttons in a uniform fashion. We modeled a fixture design that would orient the bonding button face upward, holding it level to the fixture's top face. This would ensure a constant epoxy thickness between the buttons and ceramic, and any excess epoxy would overflow without adhering to any additional sample surface area. We rapid prototyped this fixture in ABS plastic with a Makerbot Replicator 2X (Fig. 26).

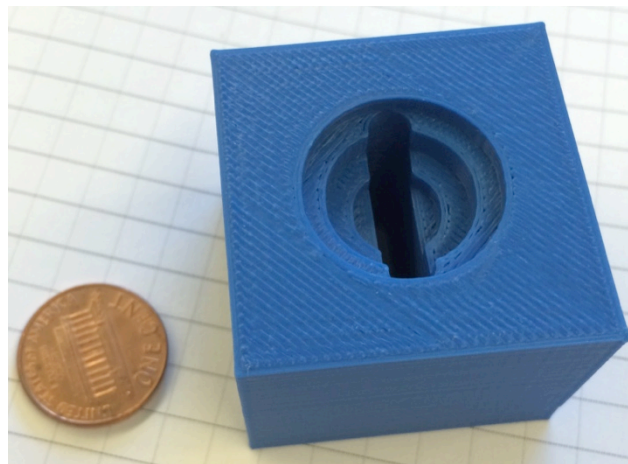


Figure 26. Rapid-prototyped gluing fixture. The counterbores were designed to accommodate the various radii and fillets of the buttons. The shallowest hole accommodates potential epoxy overflow.

Though the prototype was appropriately sized to hold the buttons, its polymeric composition could pose issues in cleaning off epoxy overflow. The typical epoxy removal solvent is acetone, and ABS is commonly treated with acetone to decrease surface roughness of parts. Therefore, we needed to use a less reactive material to viably implement the gluing fixture design. We chose aluminum for this purpose, as scrap was readily available and the metal is relatively easy to machine. We cut the flat sections of the fixture from a scrap aluminum plate and made vertical spacers from rectangular tube stock. We used a mill to drill the counterbores in the plates' surfaces (Fig. 27). When assembled, the plate and tube sections supported test buttons as well as the prototype, though the stem section was not rotationally locked as it had been in the prototype fixture (Fig. 28).



Figure 27. Machined aluminum gluing fixture parts. Some dimensions were changed to reflect the limited endmill sizes available.

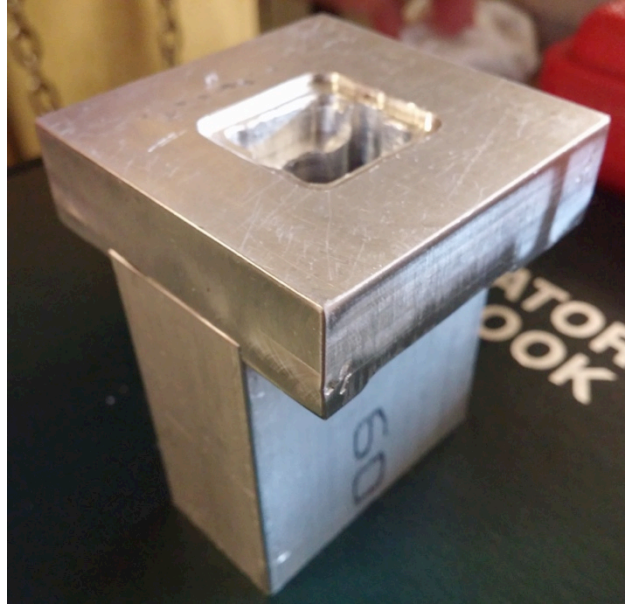


Figure 28. The assembled aluminum fixture. The hollow supporting bar provides enough space for the button stem to hang vertically.

Though the aluminum gluing fixture had all the correct dimensions for holding and gluing buttons to samples, we only managed to fully machine a single complete fixture. The full machining process took several weeks to complete, and machining more fixtures would only increase this production time. Moving forward with the single fixture we completed would require waiting for each individual sample to cure for 24 hours. When extrapolated out to sample sizes of 15 to 35, preparing full sample sizes could take anywhere from two weeks to a month. These constraints could not be accommodated in our project scope, so we retired the gluing fixture concept.

C. Sample Preparation Procedure Development

1. Determining Epoxy Volume and Application Method.

A. Initial Hand-Application Trials

As soon as we got the buttons, we began experimenting with applying epoxy. To avoid wasting samples, we hand-applied epoxy to pieces of cardboard. We cut out nine squares of cereal box cardboard, cleaned the buttons in acetone, and epoxied a button to each square with a craft stick. The epoxy was much more viscous than expected, which made applying a uniform layer easier. Each button got a different amount of epoxy. We scraped some layers to a relatively uniform thickness with the craft stick, and left others uneven. All samples cured for 41 hours.

The epoxy takes 3 days (72 hours) to reach full strength, but only 24 hours to reach 90% strength.

The ideal epoxy application method fully bonds the button to the sample surface without much epoxy overflow. Only 1, 6, and 9 from the first trial had no overflow (Fig. 29), 8 had some that is not visible below.



Figure 29. First button and epoxy trials on cardboard with all 9. Only 1, 6, and 9 did not have excess that spilled onto the cardboard around the button. Because they had enough extra epoxy to slide, 4 and 5 had too much.

After tearing each button from its cardboard, all bonds aside from 1, 6, and 9 had enough epoxy for the bond to cover the entire button surface (Fig. 30). Cardboard worked well for this test because it peels apart in layers. Table I summarizes the trial variables and outcomes.

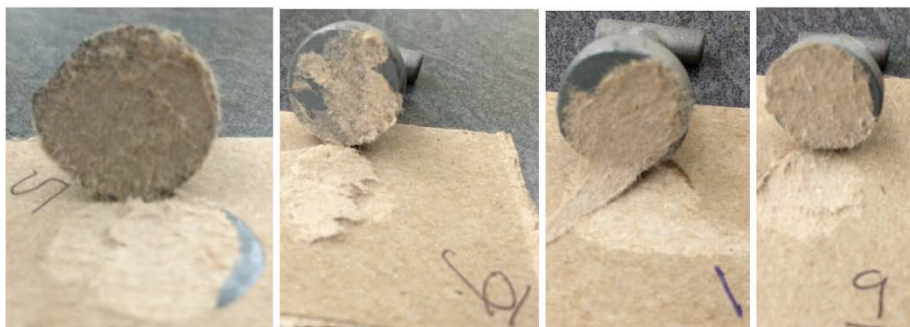


Figure 30. Bonding areas from first epoxy trials. Button 5 had excessive epoxy, but the whole surface bonded to the cardboard. However, the epoxy on buttons 6, 1, and 9 clearly did not bond the whole button-cardboard interface.

Table I. Epoxy Application Variations and Bond Completeness

Sample	Application method	Overflow	Bond area completeness and slide
1	film spread evenly, scraped excess	no	About 20% non-adherence, no slide
2	'painted' thicker layer, still thin, no scraping	some	complete, no slide
3	'painted' thinner layer than previous, no scraping	some	complete, no slide
4	larger volume, 'heaped'	much	complete, slide
5	thin coat with glob in middle, squished to sample	much	complete, slide
6	coat scraped as thinly as possible	no	About 30% non-adherence, no slide
7	larger volume, scraped to medium thickness	some	complete, little slide
8	pressed and twisted button directly in boat	some	complete, little slide
9	pressed and twisted button in thin layer on stick	no	No bond on one edge, no slide

These results showed that while hand-applying the epoxy was possible, it was not ideal. Our first tests on actual samples verified the need for a repeatable process.

After the cardboard tests, we ran initial tests on the samples (Fig. 31). We rinsed four buttons with acetone and epoxied them to the samples before letting them cure for three full days. Samples N1 and N2 used new buttons, and samples R1 and R2 reused buttons from the cardboard tests, after we removed the epoxy with acetone. We used a 0.67 g of epoxy total for these four samples, and N2 and R2 used less than N1 and R1.

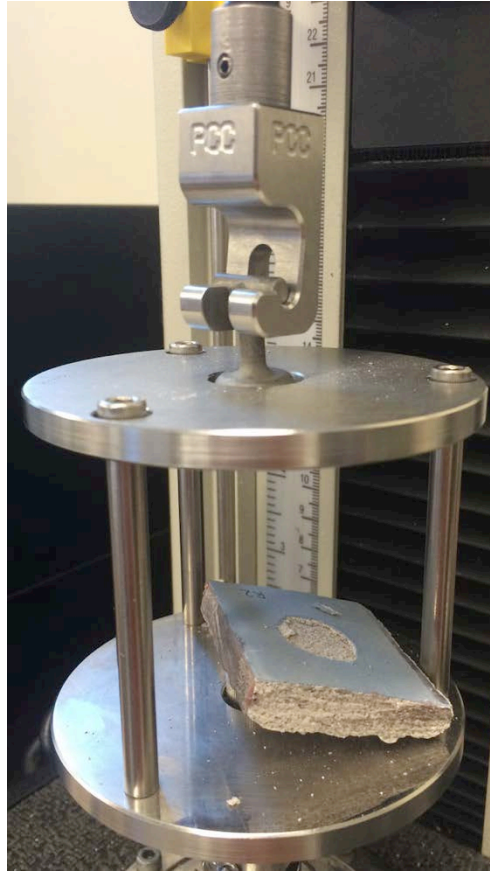


Figure 31. Initial ceramic and epoxy test. A successful pull-off test for sample R2.

All four tests broke off the first three shell layers at a crosshead displacement rate of 0.05 in/min. Sample N1 approached the 112.4 lb_f load cell limit without breaking. We stopped the test, but did not relieve the load, and the sample broke about 15 seconds later. This is an unreliable failure method, so the data point cannot be used for spalling load analysis. The other three samples all broke during testing, as expected. Note that N1 and R1 broke at high loads (Table II), while N2 and R2 broke at loads closer to those shown in the Ransom and Randolph study.

Table II. Maximum Loads from Initial Pull-Off Tests.

Sample	Maximum Load (lb _f)	Approximate Diameter (in)
N1	96.65*	0.75
R1	90.19	0.73
N2	57.62	0.70
R2	74.56	0.69

These results showed that the failure load depended on the epoxy bond area. Samples N1 and R1 had too much epoxy, which overflowed around the button. The fixture interfered with the overflow on N1 and caused it to fail at a higher load, shearing through the epoxy and delaminating the button (Fig. 32). Since R2 and N2 had less epoxy and slightly less overflow, they broke at lower loads. While testing ceramics inevitably involves some scatter, the sample preparation must be repeatable in order to minimize user-induced scatter. Hand-applying the epoxy is not repeatable enough, based on these initial results. To regulate and normalize the future tests, we decided to apply a set volume of epoxy to each button with a syringe, and measure each failure's surface area to calculate its stress. These steps kept the area more similar, and normalized the data.

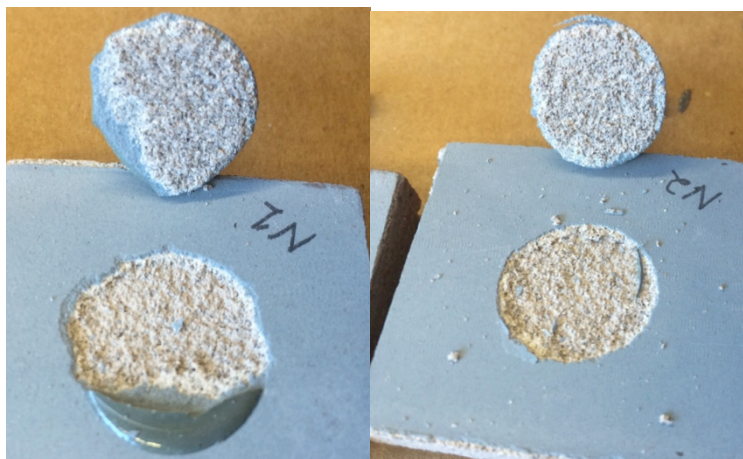


Figure 32. Epoxy overflow vs. proper volume application. Comparison of a sample with high overflow to a sample with low overflow. The overflow on N1 led to high load readings and epoxy shear while N2 only tested the ceramic bond strength. All four of the initial tests broke deeper than expected, through the face coat and secondary coats into the backup layers.

B. Epoxy volume development

In the first trial with controlled epoxy volumes, we found that 0.05 mL was the smallest repeatable amount we could apply with 3 mL syringes. We tried applying 0.1 mL of epoxy, but it had too much overflow to be valid for the final testing procedure. Figure 33 shows these eight samples. The first two buttons attached with 0.05 mL of epoxy slipped, spreading it around the sample outside of the button. By balancing the other samples before attaching the buttons, we kept epoxy from spreading outside the button too much.



Figure 33. Modified epoxy volumes and leveling. Five of the seven buttons attached with 0.05 mL stayed put and had little sliding with no overflow, and 6th and 7th moved some. Sample 8 has 0.1 mL of epoxy, and had unacceptable overflow.

After applying the epoxy, we let the samples to cure for 48 hours before testing them at 0.05 inches/minute. At this time the Instron Mini 55 was experiencing a random load frame error, and shut us out of the machine after we tested five of our eight samples. However, we determined that mitigating epoxy spreading and overflow successfully prevented tests from exceeding the load cell's limit. These loads were slightly more regular than the first tests, ranging from 56.49-87.69 lb_f. While the delaminated areas attached to each button still broke deeper than expected, these tests showed that with a repeatable sample leveling procedure, 0.05 mL should work.

To verify that 0.05 mL of epoxy worked, and develop a leveling procedure, we prepared ten samples, five with a dot of epoxy (group B), and five with 0.05 mL of epoxy (group C). We inspected each ceramic coupon for raised edges and removed them with abrasive paper. To prevent the buttons from sliding, we leveled each sample by mounting it on modeling clay and

cardboard in a leveling press (Fig. 34). With a smaller volume of epoxy, we hypothesized that we would see shallower failures, possibly before the third coat.

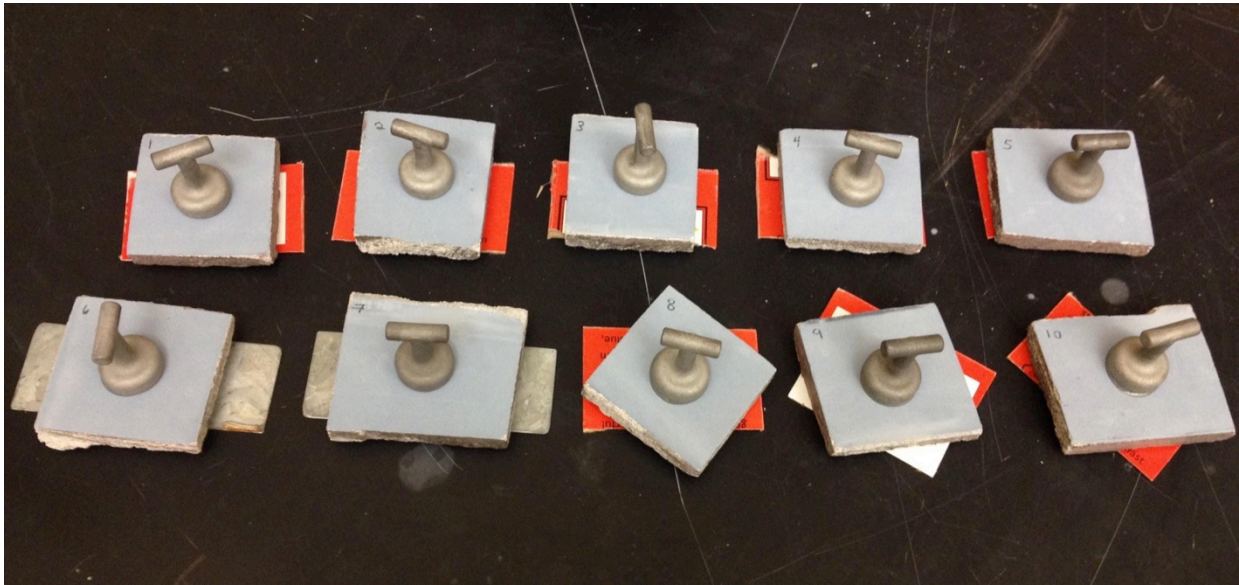


Figure 34. Leveled epoxy samples on backing. The top five samples (group “B”) have a dot of epoxy, reducing the pull-off area. The lower five samples (group “C”) have 0.05 mL of epoxy.

We tested these samples and the three original 0.05 mL samples from the previous group, which we designated Group A. While the dot samples still separated between the deeper backup layers, they left more of the second layer attached to the sample (Fig. 35). This separation between the first and second layers is more similar to the failures presented by PCC.



Figure 35. Tested samples from epoxy variations. The three groups of samples by name. Group A (top row) and group C (middle row) show patterns similar to previous tests. Group B (bottom row) showed a higher proportion of separation between shallower layers than the larger area samples.

Based on the variation in bond area on each sample even with the syringe applicator, we decided to calculate and compare failure stresses rather than loads. To do this, we used Photoshop software to measure the fracture areas of these first samples. With the program's selection and analysis tools, we scaled images of the samples to inches and measured the total fracture area. The failure stress for each sample is its failure load divided by the fracture area.

The lowest average stress was in Group A with 166.5 psi. Group B had the highest average stress with 232.9 psi, and Group C had an average stress of 186.1 psi, which was closer to the stresses in Group A. Based on these results, we prepared another set of balanced samples with 0.05 mL of epoxy (Group D, average 180.7 psi), to confirm that we had developed a procedure that produced repeatable data. As Figure 36 shows, the data was similar. While group D had more variation, it also had twice as many samples and we struggled with balancing them because the table we used was not level. With a level curing table for the epoxy, we felt we could continue getting comparable results. With this, we felt confident moving on to validating that the fixture and procedure could measure differences in strength between different shells.

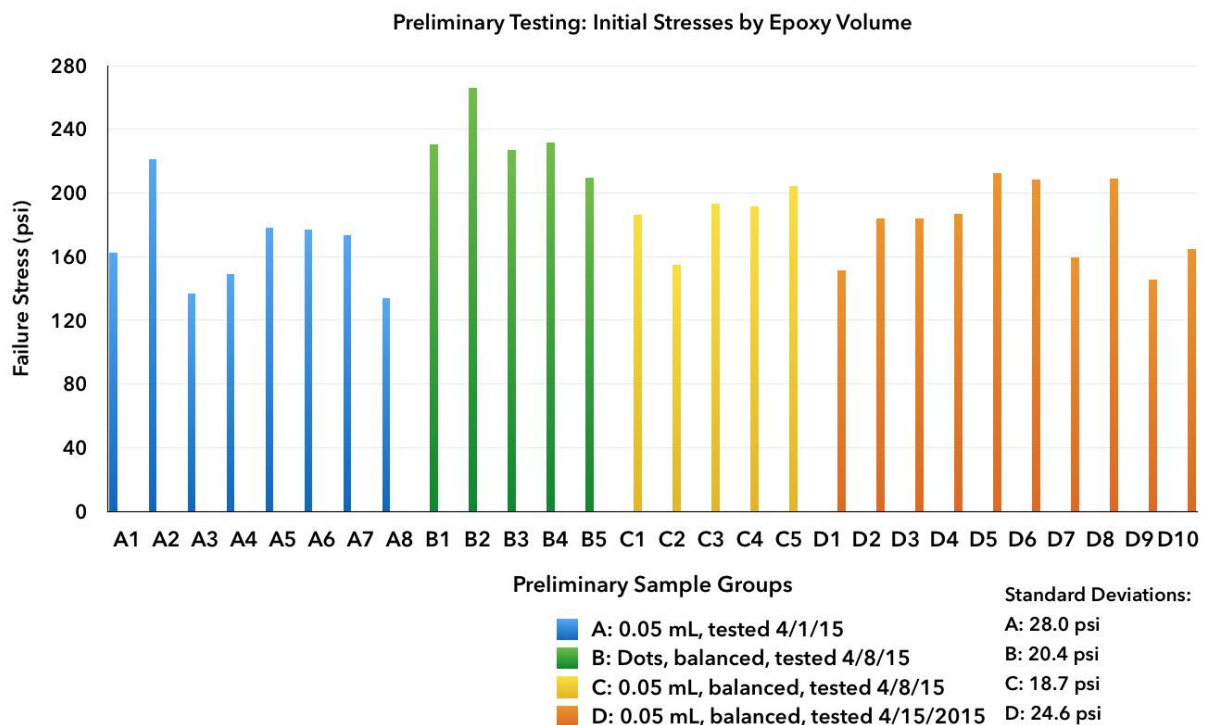


Figure 36. Failure stress plot for epoxy variations. These data points for preliminary groups A-D showed that using 0.05 mL of epoxy on leveled samples was repeatable enough to proceed with validating the test.

2. Tape Test

Because the failures were all deeper than expected, we attached buttons with double-sided mounting tape to see if the epoxy was seeping through the first two layers. We thought we might be able to force spalling by using an adhesive that only bonded to the sample's surface. After attaching the tape to the buttons and coupons, we held them together for 30 seconds as advised by the packaging. We tested one sample at the same 0.05 in/min crosshead movement, the same as for those bonded with epoxy, but tape peeled off both the button and sample without removing any of the face coat. While the tape was unsuccessful, the hook realigned itself to continue pulling perpendicular to the bond (Fig. 37), with no signs of removing any layers of the ceramic. While using tape may warrant more investigation in a future project, we kept using the epoxy.

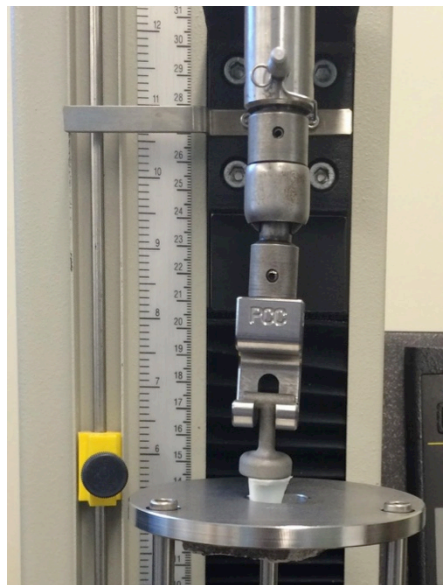


Figure 37. Attempted foam tape test run. The tape both peeled and stretched during testing, while the hook re-aligned itself to pull normal to the tape surface. This resulted in the hook holding the button off to the side of the testing hole.

3. Photoshop Measurement

To measure the fracture surface area of the samples after testing, we used Photoshop. This required a photo parallel to the sample, making the point of view perpendicular to the smooth test surface, and including a scale in the image to reference the measurement. Photoshop has analysis tools that can set the scale of objects in the imported image with respect to the

photographed scale. The scale modification tool is found in the path “Image > Analysis > Set Measurement Scale > Custom...” (Fig. 38). After setting the “Logical Units” field to “Inch”, draw a line designating a linear distance of one inch according to the image (Fig. 39). After hitting “OK”, the program directly converts pixel measurements to inches.

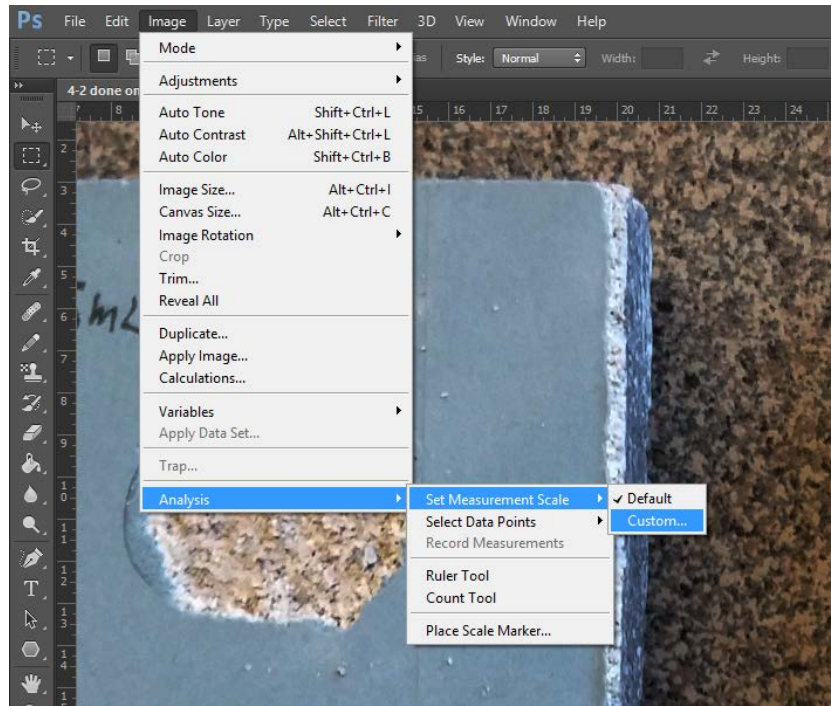


Figure 38. Process of scale modification in Photoshop .The menu path to the scale modification tools, which are used to set logical scales of reference within an individual image.

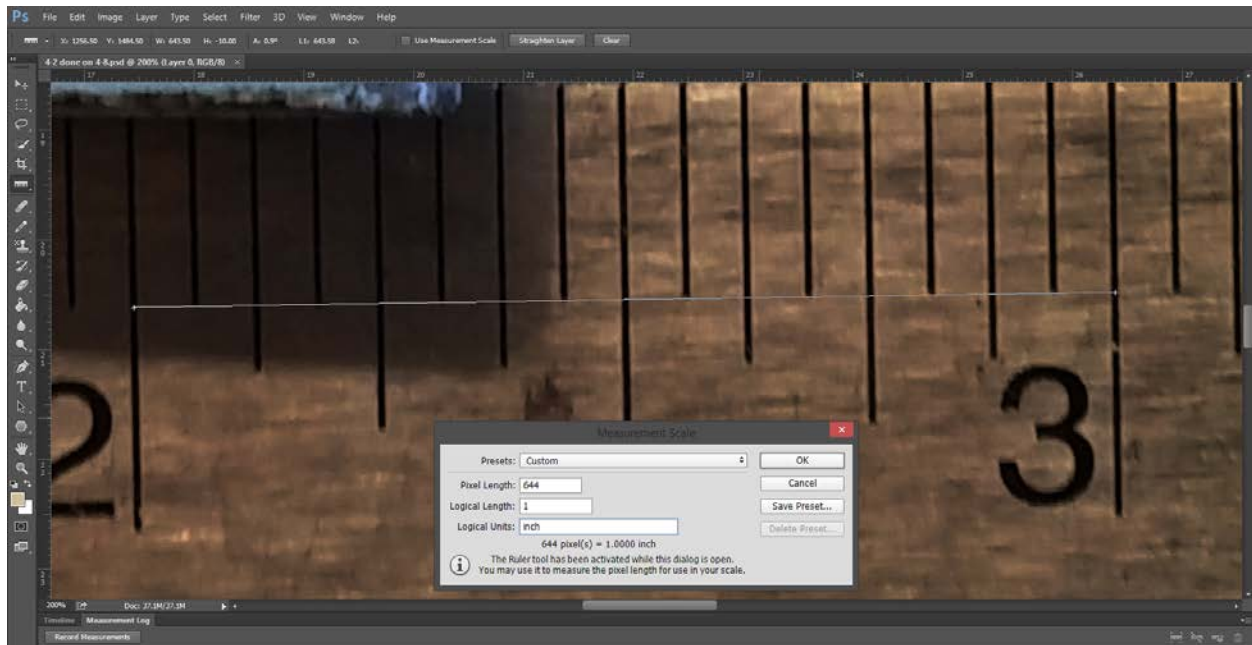


Figure 39. Calibration of the scale in Photoshop. Manual scale setting using the Measurement Scale tool. The user drags a line between two points and defines the pixel length as a distance in terms of a logical unit such as inches.

Most images needed contrast and brightness adjustments to clearly define the fracture zone edges, which simplifies selecting the area with one of Photoshop's built-in pixel selection tools. After adjusting the image, the "Quick Selection Tool", which automatically distinguishes between appreciably contrasting colored areas, was most convenient for this purpose. All edges were carefully selected and refined using this tool, to accurately measure the full fracture area. The user then clicked the "Record Measurements" button in the "Measurement Log" region at the bottom of the screen (Fig. 40), and the log displayed the selected area in inches squared. Each sample's failure stress was calculated from the failure load divided by the area.

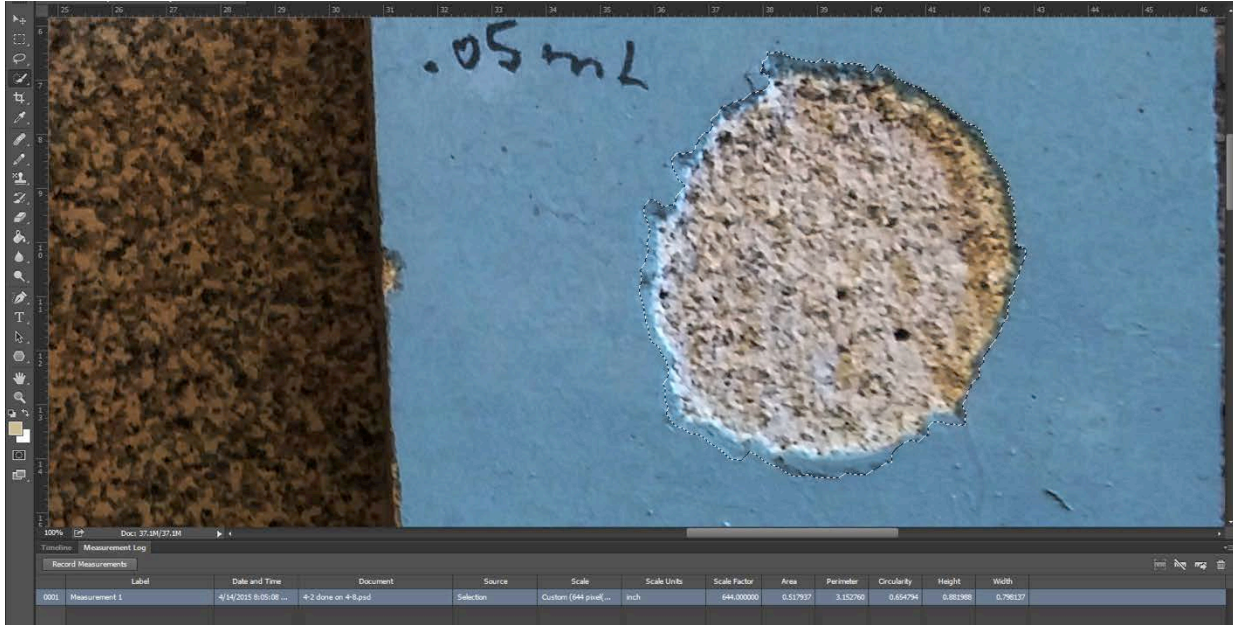


Figure 40. Area measurement in Photoshop. The fractured area, selected using the Quick Selection Tool, is shown inside the dotted line on the image. The measurements of this area are calculated in the Measurement Log region at the bottom of the window.

D. Fixture Validation Design of Experiment

After establishing a functional procedure with the first 35 samples, we began testing shells that should have differences in strength, to determine whether the test could detect these differences. We used 36 standard green shells (Group A), 18 fired standard shells (Group B), and 35 green shells with a double layer of the second coat, which still uses fine refractory flour (Group C). The fired shells were known to be stronger than the green shells, so they were meant to clearly show whether the fixture worked correctly. While testing more of the fired shells would have provided an advantageous set of data, we used a small sample size because they were mostly meant to show that the fixture could measure expected differences in strength. Additionally, they came from the same processing as Group A, providing a direct comparison to see whether the bond to the face coat weakened during dewaxing and firing. Group C's construction has been used in the past to prevent spalling, so we hoped that it was quantifiably different from Group A.

With a 112 lb_f load cell, we were concerned that the fired samples might be too strong. Before beginning the full test, we prepared three samples from Group B with 0.05 mL of epoxy, and 3 with a dot of epoxy attaching the button to the shell. When we tested these samples after

48 hours, the highest loads (78-80 lbs) were well below the load cell's limit. The loads from samples with epoxy dots were low, while loads from samples with 0.05 mL of epoxy were in the same range as some of the green shells. Both groups had similar stresses, but the samples with epoxy dots did not fully separate from the buttons when the shells failed, leaving the button attached by friction between the two fractured faces. Since the loads from samples with 0.05 mL of epoxy were safe for the load cell, we decided to continue preparing samples with this epoxy volume.

E. Final Procedure

Based on the above procedure development, we determined that the bond area depends on the volume of applied epoxy, and the samples must be completely level to prevent the epoxy from spreading. Our final procedure began with rough-cut samples. These often had a raised edge from the saw that we ground off with abrasive paper without touching the center of the sample's surface. For the final tests, we photographed each sample's surface before epoxying to record any variations and defects for reference during analysis (Appendix A). Figure 41 shows the steps to tensile test each sample. After this, the samples are analyzed in Photoshop to measure area, and we photograph the buttons under a stereoscope to record the failure surface (Appendix B).

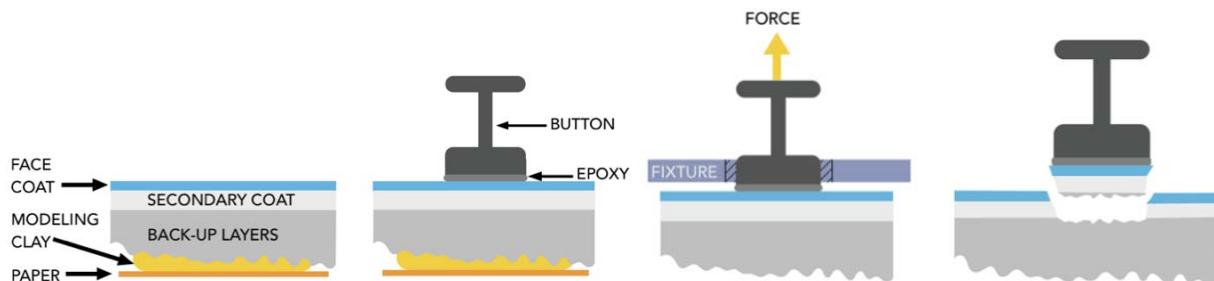


Figure 41. Steps of sample preparation. Because of the samples' uneven backup coats, each must first be leveled on modeling clay and put on a level surface. A 3 mL syringe is used to apply 0.05 mL of Hysol Loctite 9340 epoxy to the button, which is then placed on the sample. After 48 hours, they are tested at 0.05 inches/minute until failure. The sample's strength is the failure load over the failure area measured in Photoshop.

IV. Shell Comparison

A. Testing

We prepared 83 samples with 0.05 mL of epoxy each. To prevent the buttons from sliding, we leveled a glass shelf, and put all the leveled samples on it before applying the epoxy (Fig. 42).



Figure 42. Leveled glass table with fully prepared samples, in the setting process.

During sample preparation, we noticed that 11 of the Group C shells had cracks in the face coat (Fig. 43). Most of these cracks were not underneath the epoxied area, but we recorded the locations so we could check if they affected testing. Samples in all three final test groups also exhibited different degrees of speckling on the face coat.

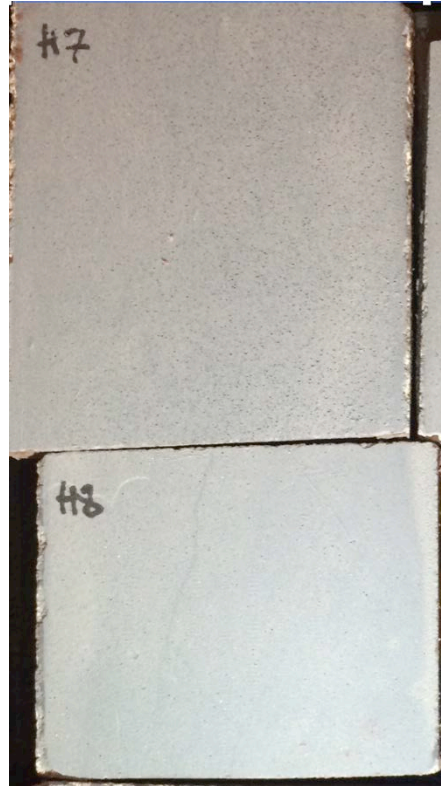


Figure 43. Pictures of surface cracks. These samples from “Group C” were labeled as Group H during testing to continue an alphabetical naming scheme. “H8” had a crack down the middle of its left side, while “H7” was not cracked. Additionally, “H7” displayed a medium degree of surface speckling, while “H8” displayed little-to-none.

These 83 samples took two syringes of epoxy. The first batch of epoxy sat in the syringe for about 10 minutes after mixing while we cleaned the buttons. This slightly cured epoxy was easier to work with when attaching the buttons, because of its increased viscosity. While preparing coupons, we randomly alternated between Groups A and C to ensure consistency. Group B was prepared last.

During testing, we formed a random sample queue for the sample order to avoid bias and to eliminate differences in loading. Each test ran at a crosshead displacement rate of 0.05 in/min. We performed the tests in three separate trials, all within 48-72 hours of sample preparation. Each test took approximately 45 seconds.

For a quantitative measure of different failure modes, we measured the depths of a representative set of failures with an optical microscope. To ensure that measurements were perpendicular to the surface of the sample, samples were carefully re-mounted on modeling clay, to level the face coat surface. Each sample was measured at multiple locations. Data point were

the distance between the deep and shallow focal lengths, zeroed at the sample's surface. The focal boundaries were set where approximately one-quarter of the area came into focus.

B. Results

1. Failure Modes

In these tests, we had 6 samples that failed mostly in the face coat (C1, C16-C18, C23, C27), all from Group C (Fig. 44). Groups A and B appeared to fail either with a relatively flat break through the back-up layers, or a more varied break that went up and down through several layers. Group C failed in three ways, either shallow in the blue face coat, deep through several layers, or more similarly to the flat ones in Groups A and B. The deep failures broke so that the shell attached to the button formed a rounded mound, extending down approximately $\frac{1}{8}$ " into the sample. All these failure types are categorized in Table III, and Appendix C contains more data on their stresses by group and type.

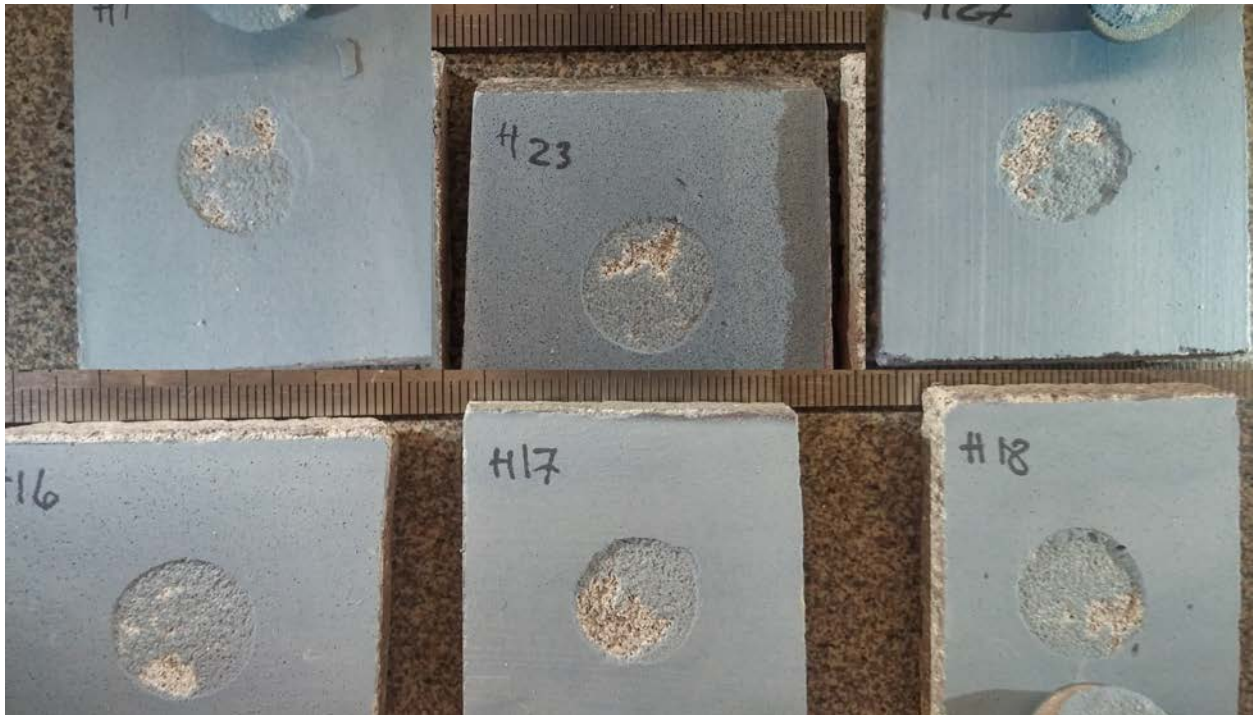


Figure 44. The expected "typical" spalling failure. Six samples that displayed ideal spalling behavior during testing. All samples belong to group H.

Table III. Details on Failure Modes.









<p>Blue, shallow. Layer 1-2 N=6 Group C only</p>		
<p>Flat Layer 3 $N_A=17, N_B=8$ Groups A and B</p>		
<p>Deep Layers 4+ N=14 Group C only</p>		
<p>Middle Layers 3-4 $N_A=19, N_B=7, N_C=15$ Groups A, B, and C.</p>		

Figure 45 shows the depths of the failure types measured on the optical microscope. The right-hand side of the graph approximates each layer's depth, physically describing the numerical depth.

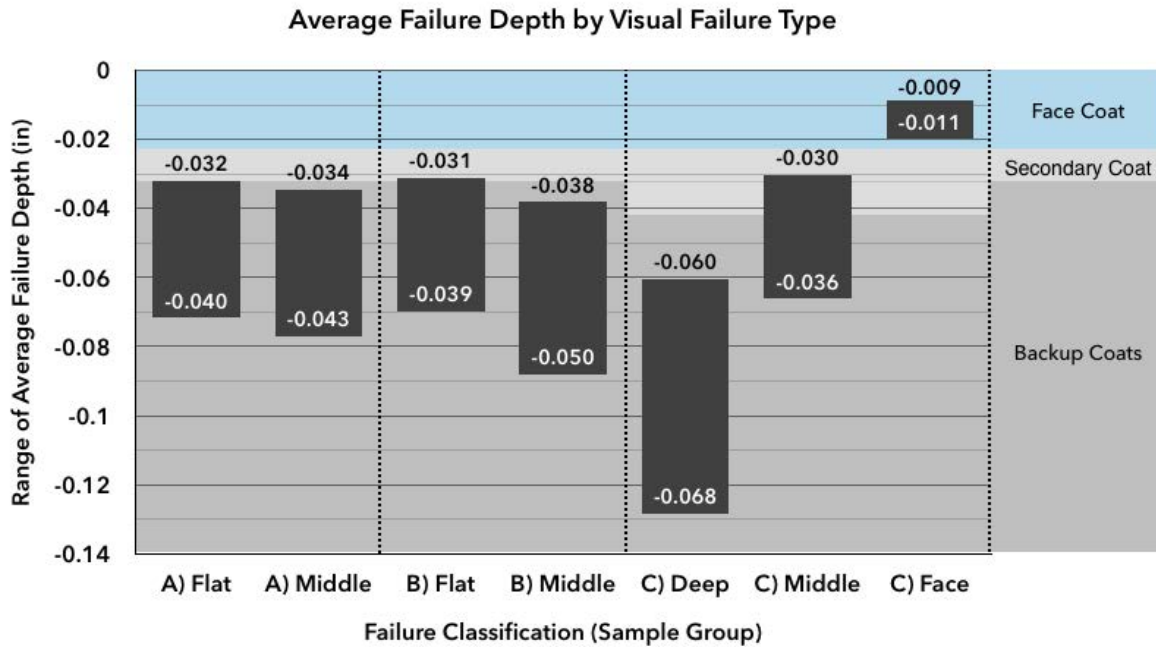


Figure 45. Quantitative depths of seven visual failure types. The five middle failures are generally in the same range, except for the partially fired samples where larger stucco is visible.

We applied the calculated stresses to the different visual failure modes (Fig. 45) to see if they affect the stress (Fig. 46).

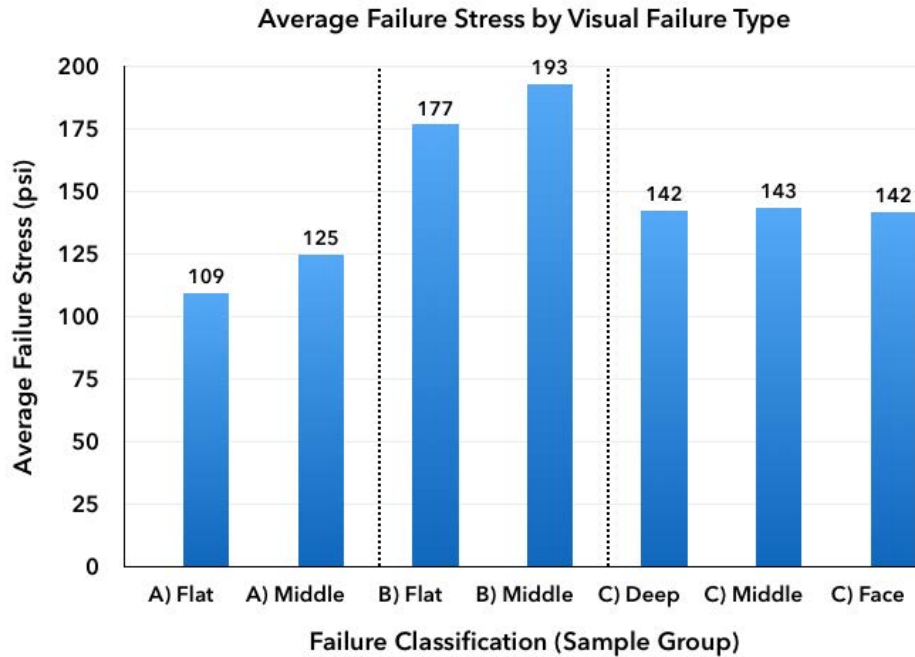


Figure 46. Average stresses of failure modes. These average stresses are in the same right-to-left order as the sample groups in Figure 2, to show how depth variations affect stress. Note that the depth variation in Group B seems to have not affected the stress, while Groups A and B both vary by about 20 psi between the small particle flat and stucco-visible failures.

We tested these seven groups for equal variance, and they passed with $p = 0.415$. This allowed us to run an ANOVA. The Tukey results are in Table IV by group and failure mode. Each mode's stress interval is plotted in Figure 47, where the first letter (A, B, or C) designates the group, and the second letter (M, F, B, or D) designates a middle, flat, blue, or deep failure.

Table IV. Tukey Groupings for Stresses by Failure Mode.

B. Middle	B. Flat	C. Deep	C. Middle	C. Flat	A. Middle	A. Flat
A	A					
	B	B				
		C	C	C	C	
				D	D	D

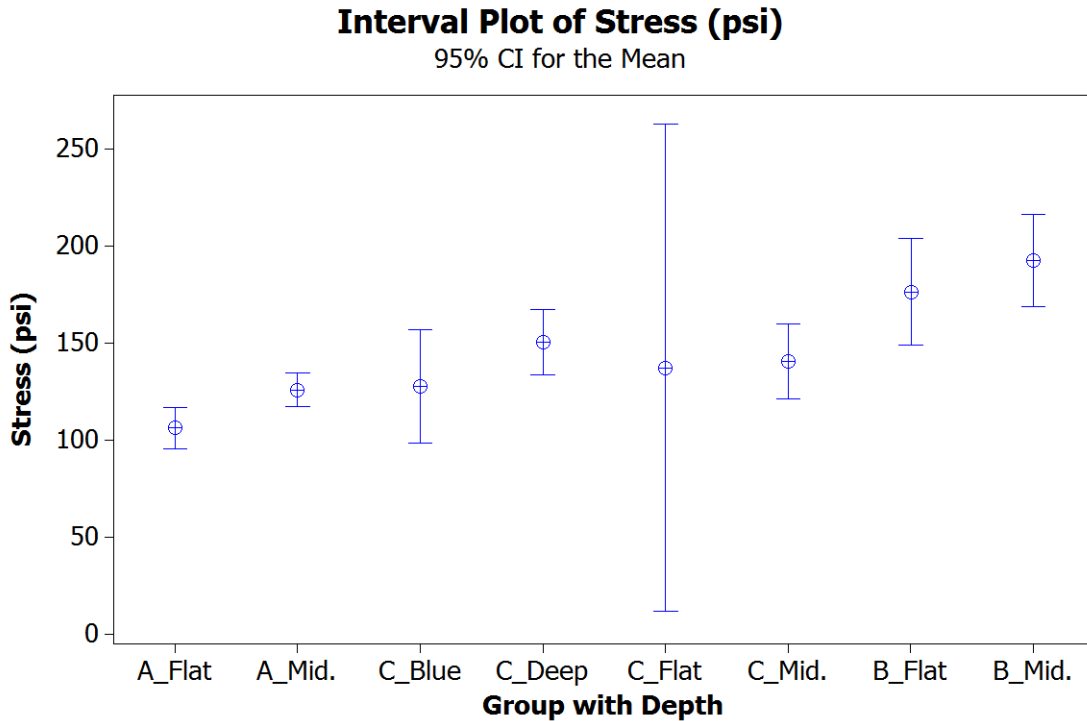


Figure 47. An interval plot of stress by failure modes, showing the 95% confidence interval and mean of each mode's stresses.

To determine if the data matched the ANOVA model, we stored the residuals from the ANOVA and tested them for normality. The residuals are left over after fitting the data to a normal curve, and show whether the data has significant outliers, or lacks normality. The normality test linearizes a cumulative normal distribution curve and plots a data set against this line. These standardized residuals fit the line.

2. Pre-existing Surface Cracks Visual Results

Table V shows details on the cracked samples, both before and after testing. Additionally, the specks observed on some samples seem to not be related to how they failed (Appendix D).

Table V. Effect of Pre-Testing Surface Cracks on Failures.

Sample	Crack location	Failure Stress (psi)	Failure Depth	Crack's Proximity to Failure
C4	right edge	153.8	Middle	Crack far from break
C6	middle-top	117.5	deep to blue	Crack near deep edge
C8	left-center	135.6	middle	Crack through break
C12	center	119.1	deep to blue	Crack through
C14	bottom center up	193.7	normal	Crack into break
C15	towards center	175.6	normal	Crack into break
C21	up right	130.3	deep	Crack into break
C22	center	129.1	deep	Crack into break
C26	left side	144.1	deep	Crack into break
C29	center	166.3	normal	Crack around break
C33	top left to middle right	162.2	normal	Crack through slightly deeper corner

3. Testing for Results by Group

After testing the failure groups, we determined whether the three sample groups' strengths were statistically different from each other. Figure 48 shows our test for equal variance, which . This test shows whether the groups' standard deviations are comparable. Its null hypothesis claims 95% confidence that the standard deviations of the groups are equal. This returned $p = 0.1$, large enough that we cannot reject it, and may consider the groups equally variant. With effectively equally variant groups, we ran an ANOVA to test our null hypothesis that the mean stress for all three groups was equal. Table VI shows these results, which gave a p-value less than .001, clearly stating that the groups have different stresses. To confirm that the means for each group were different, we drew up an interval plot (Fig. 49). The standardized residuals from this test also fit the normal line (Appendix E), affirming that the ANOVA is a valid analysis model for this data.

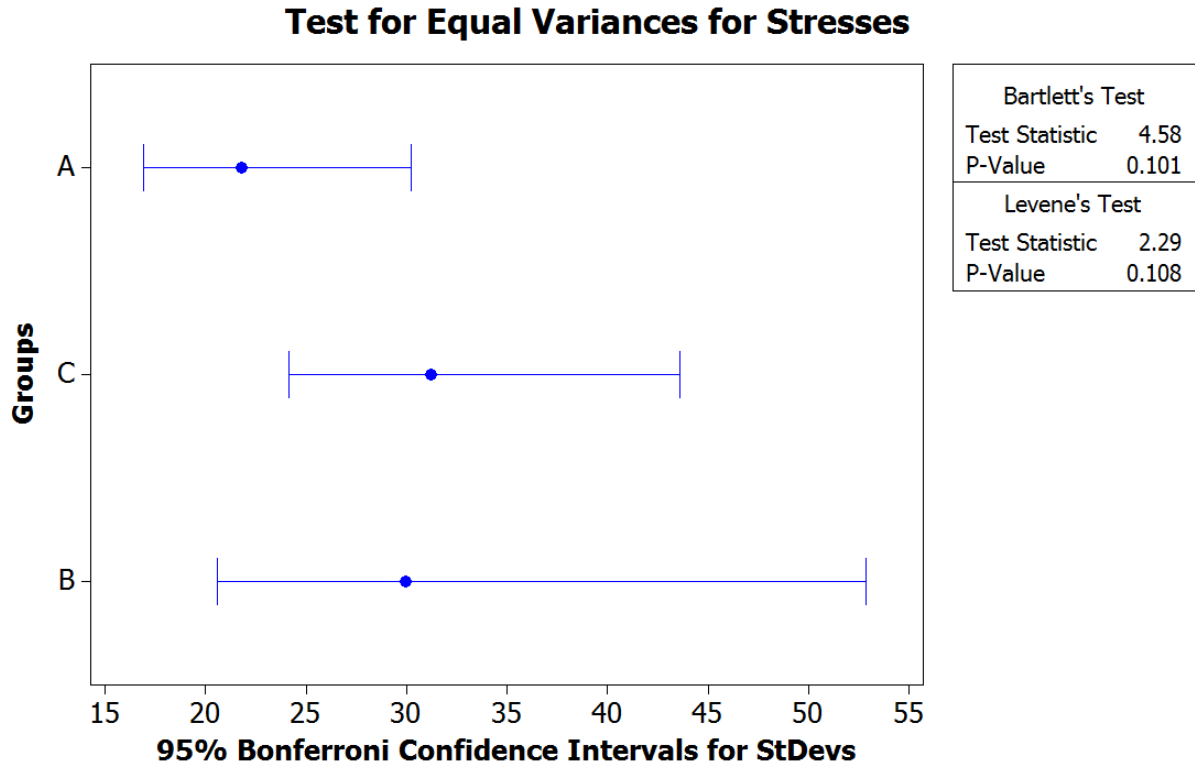


Figure 48. Equal variance test for groups' stresses. These intervals show the intervals where each group's standard deviation can be found 95% of the time.

Table VI. ANOVA Results for Failure Stresses by Sample Group

Sample Group	N	Mean Stress (psi)	Standard Deviation (psi)	Tukey Grouping
A	36	116.2	21.8	3
B	35	141.2	31.2	2
C	12	184.2	30.9	1

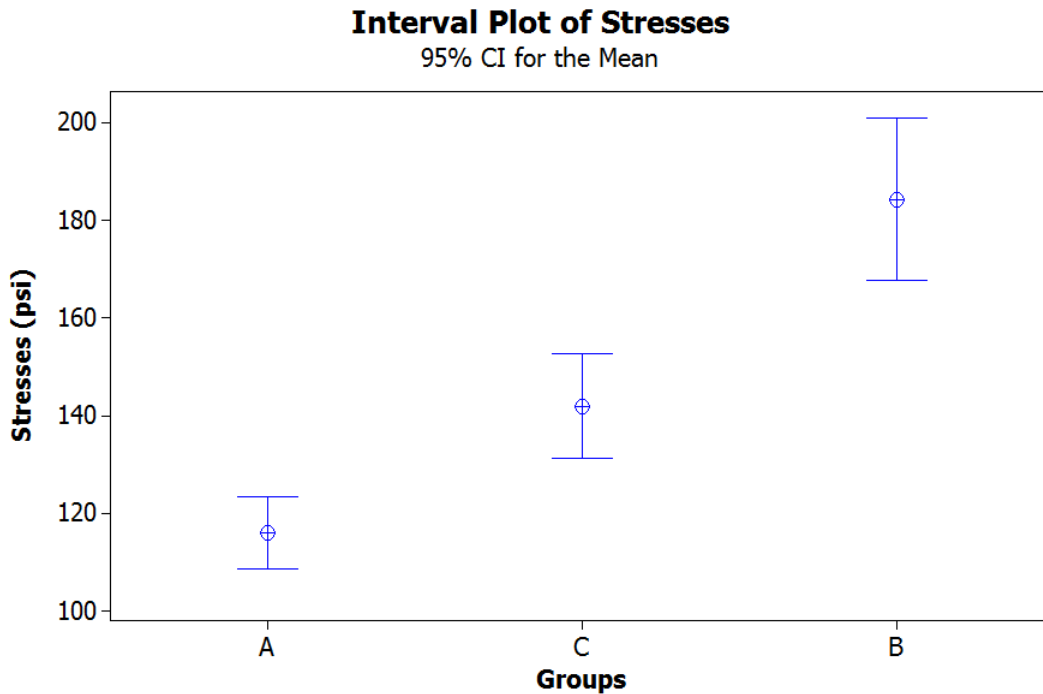


Figure 49. Interval plot of the group's stresses. The 95% confidence intervals for each group's mean stress shows that each group has its own distinct range of failure stresses.

C. Analysis

1. Depths

Although the visual failures looked different from each other, they failed similarly. Groups A and B showed little difference in measured depth, just enough to illustrate that the middle failures went deeper than the flat ones, into the next stucco coat. The middle failure in Group C was comparable to those in Groups A and B, while the deep and face coat failures were entirely distinct. Because of these differences, we expected to see at least some variation in the failure stress of each mode. In Group A, the flat failures had one low sample, (A4, 65 psi), and the middles had one strong sample (A28, 169 psi) that were outside of the other mode's range. However, the other 34 samples failed in the same ranges, regardless of mode. The same is true of Group B, where the flat samples had one low failure (B4, 112 psi), and the middle samples had one high failure (B14, 225 psi). Three of the middle samples in Group C failed higher than samples in the blue or deep failures did (C14, C15, and C25, at 194 psi, 175 psi, and 209 psi, respectively), but there were no surprisingly weak failures. In both Groups A and B, the average

stresses for flat failures was 16 psi less than the average for middle failures. In Group A, this was 109 psi compared to 125 psi. With a standard deviation in this data of 21.8 psi, this difference is not significant. Group B had flat samples with an average strength of 177 psi, and middle samples at 193 psi. This 16 psi difference in a data set with a standard deviation of 30.9 psi also showed no significant difference in strength by failure depth. Finally, the averages for Group C's blue, middle, and deep failures were 142 psi, 143 psi, and 142 psi, respectively. In a data set with 31.2 standard deviation, these 0-1 psi differences clearly show no change in strength by depth.

The Tukey grouping results from Table IV also do not show a clear trend between depth and failure stress. All modes in a respective group did statistically the same, and the partial overlap between groups is not concerning because that is not the metric for which the test was designed. Based on the graphical and statistical results, we determined that while the different failure modes were concerning, they did not affect the strength results.

2. Surface Cracks

We expected the cracks through the failure areas to increase the depth or decrease the failure stress. However, the cracked samples had the same range of stresses and depths as the ones with the whole face coat. Cracks went through five of the normal or middle-depth failures, three of the deep failures, and one of the samples that broke both in the face coat and deeply. The range of stresses matches that of the overall group, from 117.5-193.7 psi averaging around 147.5 psi. This average is only 6.3 psi higher than the average of the whole group, not significant enough to determine an effect from the pre-existing cracks in the face coat.

3. Difference by Groups

Based on the above analysis, we determined that we could treat the sample groups themselves as the only factor in measuring for differences in strength. As expected due to their different constructions and fired states, Groups A, B, and C had different strengths. Because the test for equal variances had a p-value of 0.1, too large to reject, we may consider the three sample groups equally variant. The overlap between groups on the variances plot (ref. Appendix) confirms this.

According to the Tukey comparison results (Table VI) from testing for differences in strength between the three groups, the groups are statistically different from the others. This is because they were not assigned the same Tukey label, and groups that do not share a label are statistically different. The GLM showed that Group A was the weakest and Group B the strongest (Fig. 49). Group A's mean is 25.8 psi weaker than that of Group C with individual data points 10.2 to 41.32 psi weaker. Group A's mean is 68.03 psi weaker than Group B's with individual data points ranging from 47.91-88.15 psi weaker. Finally, Group B is 22.04-62.46 psi stronger than group C, with a 42.25 psi difference in their means. Figure 49 shows these intervals graphically by group. This confirms our expectation that the fired shells are stronger than the green ones. PCC has found that the additional secondary layer that Group C has makes molds less likely to spall. We measured them as stronger, which matches our original assumption in designing this test: shells are less likely to spall if they have a stronger bond between layers.

4. Materials Mechanisms

Distinct mechanisms strengthen each group. Groups A and B are green, gaining most of their strength from the colloidal silica binder that comprises 5-10% of the slurry. Water suspends these silica particles, and as the slurry dries hydroxyl groups on the particles' surfaces interact, facilitating the formation of siloxane and hydrogen bonds between particles (Fig. 50) [Golshan, Sarpoolaky, and Sour]. This provides modest strength in the unfired shell.

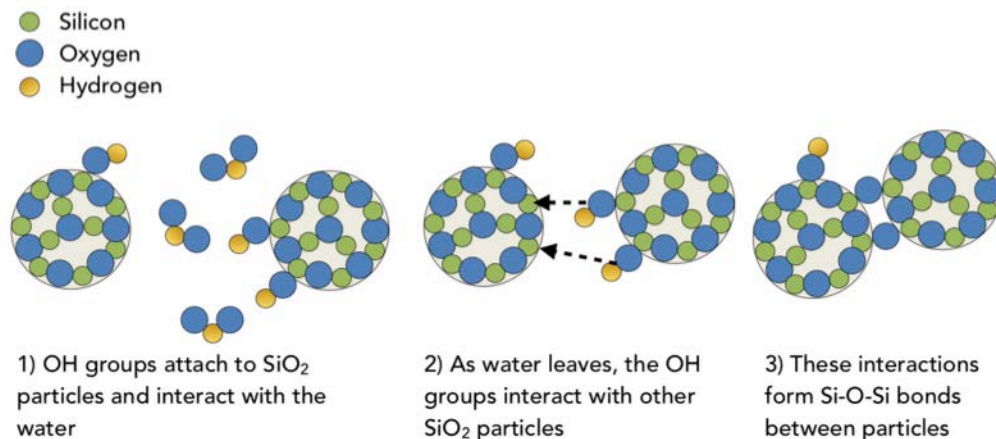


Figure 50. Schematic of how covalent bonds between silica particles provide green shell strength. [Golshan]

Group B and Group A were constructed in the same order, but Group B was also fired above zircon's sintering temperature. This drives atomic diffusion between particles, forming a solid-state with new strong ionic bonds, increasing the shell's strength (Fig. 51).



Figure 51. Diagram of the fired shell. Firing the shell allows particles to diffuse into each other, forming ionic bonds that hold the shell together more strongly than the covalent and hydrogen bonds holding the green shells.

Group C shares the siloxane strengthening of Group A, but the additional prime slurry coat increases the thickness of fine layers in the mold (Fig. 52). The fine particles of this extra layer provide a more gradual transition between the face and backup coats and have more surface contact between particles. The particles in any coat come in a distribution of sizes, and the smaller particles fill the spaces between the largest ones. However, the coats with finer overall particles pack more densely and have more siloxane bonds between particles, making them stronger. This improved bonding from the additional layer with greater density provides the 25 psi increase in mean strength from Group A to Group C.

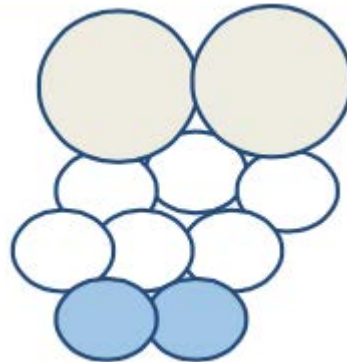


Figure 52. Diagram of shell system with the additional third layer. The fine particles in Group C's additional secondary layer provides another dense layer in the mold. This both strengthens the mold by being more dense, and by providing a more gradual transition to the large particles in the backup coats, allowing them to bond better.

V. Conclusions and Recommendations

Conclusions

1. Our test fixture and procedure repeatably measure the interlayer adhesion strength in zircon investment casting molds.
2. Shells with an additional third coat of fine particles are stronger due to increasing the thickness of the dense primary layers, which may explain why they are less likely to spall.
3. Because the stronger green shells were the ones that tend to spall less, our initial assumption that shells with stronger interlayer bonds would be less likely to spall seems to be valid, and testing this bond in tension rather than shear is permissible.
4. Our test experiences failures where they should theoretically occur, but not where the defect we want to force occurs.
5. This test may be useful in qualifying new shell systems by their strength.

Recommendations

1. Since spalling most often occurs in the corners of molds that produce small filleted radii in the cast parts, we recommend testing shells with different corner geometries to best measure the mold's tendency to spall.
2. To ensure that cracks propagate normal to the loading direction, we recommend mixing glass beads into the epoxy to maintain a uniform bond thickness across each button, and all samples.

VI. Bibliography

A. General Information

Atwood, R.C, P.D Lee, and R.V Curtis. "Modeling the Surface Contamination of Dental Titanium Investment Castings". *Dental Materials*, 21.2 (2005): 178-186.

Birben, Gurkan. "Vacuum Induction Melting for Investment Casting". *Industrial Heating*, 74.11 (2007): 63.

"Full Alloys Chart". *Precision Castparts Corp. Structural*s. 2014. Web.

LeBeau, James M, and Yuttanant Boonyongmaneerat. "Comparison Study of Aqueous Binder Systems for Slurry-based Processing". *Materials Science & Engineering a*, 458.1 (2007): 17-24.

Precision Castparts Corporation. *Capabilities*. 2014. Web.
http://www.pccstructurals.com/about_pccs/capabilities/

Precision Castparts Corporation. *Conflict Minerals Report Calendar Year 2013*. Portland, OR. 2013.

Saridikmen, H, and N Kuskonmaz. "Properties of Ceramic Casting Molds Produced with Two Different Binders". *Ceramics International*, 31.6 (2005): 873-878.

B. References Cited in Text

"Adhesive Bond Tensile Fixture (ASTM D897)". *Wyoming Test Fixtures, Inc.*

Akhavan, A.C. "Overview of Silica Polymorphs". *The Quartz Page*. 12 Jan. 2014. Web.

Bidwell, H.T. *Investment Casting*. Sussex: The Machinery Publishing Co., Ltd. 1969. Print.

"Casting Capabilities". *AlCuMet, Inc.* 2015. Web.

Chen, Y.F., S.L. Xiao, J. Tian, L.J. Xu, and Y..Y. Chen. "Effect of Particle Size Distribution on Properties of Zirconia Ceramic Mould for TiAl Investment Casting". *Transactions of Nonferrous Metals Society of China*, 21 (2011): S342-S347.

Cheng, X., C. Yuan, S. Blackburn, and P.A.. Withey. "The Study of the Influence of Binder Systems in an Y2O3-ZrO2 Facecoat Material on the Investment Casting Slurries and Shells Properties". *Journal of the European Ceramic Society*, 34.12 (2014): 3061-3068.

Cotton, J. D., L. P. Clark, and H. R. Phelps. "Titanium Investment Casting Defects: A Metallographic Overview". *JOM* 58.6 (2006): 13-6. *ProQuest*. Web. 19 Nov. 2014.

- Das, Niranjana. "Advances in Nickel-based Cast Superalloys". *Transactions of the Indian Institute of Metals*, 63.2 (2010): 265-274.
- DePoorter, G.L. Brog, T.K. Readly, M.J. Readly. *Structural Ceramics, Properties and Selection: Nonferrous Alloys and Special-Purpose Materials*, Vol 2, *ASM Handbook*. ASM International, 1990, p 1019-1024.
- Diamond, G. X. (Ed). *Investment Casting Handbook*. Chicago: Investment Casting Institute. 1968. Print.
- Golshan, N. H., Sarpoolaky, H., and Souri, A. R. "Microstructure and Properties of Colloidal Silica Bonded Magnesite Castable Refractories". *Iranian Journal of Materials Science and Engineering*, Vol. 8, No. 1, Winter 2011.
- Han, Joo-Hwan. "Joining of zirconia ceramics in a green state using a paste of zirconia slurry". *Ceramics International* 39 (2013) 239-243.
- "History of PCC Structurals, Inc". *Precision Castparts Corp. Structurals*. 2014. Web.
- Holek, D.Conrad, and Fetter, Zachary. "Evaluating Spalling Factors through Measuring Intercoat Adhesion". Ransom & Randolph. 2014.
- Horton, R.A.. *Investment Casting, Casting*, Vol 15, *ASM Handbook*, ASM International, 2008, p 646–661.
- Houivet, David et al. "Ultrafine Grinding of Oxide Powders using a Controlled Viscosity of Slurries". *Advanced Engineering Materials* 13.7 (2011): 609-613.
- Hunt, L. B. "The Long History of Lost Wax Casting: Over Five Thousand Years of Art and Craftsmanship". *Gold Bulletin*, 13.2 (1980): 63-79.
- Jackson, James D., Singh, Nipendra, and Thornton,Thomas. "Include Nothing: Step-by-Step Reduction of Investment Casting Inclusion Defects". *Modern Casting* 94.4 (2004): 35. *ProQuest*. Web. 20 Nov. 2014.
- Jones, S, and C Yuan. "Advances in Shell Moulding for Investment Casting". *Journal of Materials Processing Tech*, 135.2 (2003): 258-265
- Leyland, Steven P., and Ian Smith. "Implementing a Water-Based Shell Mold System". *Modern Casting* 88.1 (1998): 34.*ProQuest*. Web. 20 Nov. 2014.
- "Adhesive in a Tube. Loctite 9340 Chemical Resistant Epoxy, 2.7 Ounces". McMaster-Carr
- Pattnaik, Karunakar, Jha Pattnaik, S, DB Karunakar, and PK Jha. "Developments in Investment Casting Process-A Review". *Journal of Materials Processing Technology*, 212.11 (2012): 2332-2348.

“PCC Report” Precision Castparts Corporation. *Annual Report to Shareholders*. Portland, OR. 2013.

“Standard Terminology Relating to Refractories”. ASTM C 71, Annual Book of ASTM Standards, ASTM

“The Investment Casting Process”. *Alcoa Howmet*. 2015. Web

“Welcome to PCC Structural”. *Precision Castparts Corp. Structural*. 2014. Web.

“Visit Our Process”. *ALCuMet, Inc*. 2015. Web.

Yuan, C, S Jones, and S Blackburn. “The Influence of Autoclave Steam on Polymer and Organic Fibre Modified Ceramic Shells”. *Journal of the European Ceramic Society*, 25.7 (2005): 1081-1087.

Appendix A: Sample Surfaces Before Testing

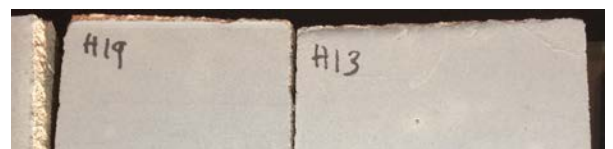
We took pictures of each sample before attaching the buttons. This showed us that some had varying degrees of “specks”, which did not seem to affect the final results. Another surface feature, which only appeared in Group C, was fine cracks in the surface of several samples. Table AI shows the comments and failure stress for each sample, while the images themselves surround the table. We did not organize the samples before taking these pictures, so there is no logical order. Note: samples are labeled with their original “G”, “H” and “I” groups. During analysis, we changed “G” to “A”, “I” to “B”, and “H” to “C”

Table AI. Pre-Test Surface Comments

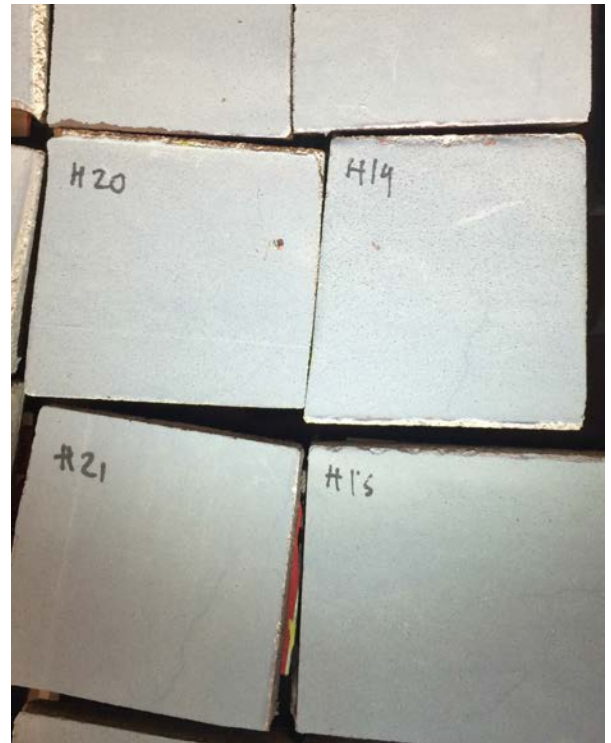
Sample		Surface Comments Pre-Test	Stress (psi)	speck heavy	speck medium	speck light	no specks
G1	A01	Uniform surface, some wrinkles	95.605				x
G2	A02	Light-medium on the blue dots	137.053			x	
G3	A03	Uniform surface	123.313				x
G4	A04	Uniform surface	81.741				x
G5	A05	Line from wax top-to-bottom along the left	100.125				x
G6	A06	Uniform surface	131.153				x
G7	A07	Medium on the blue specks, shallow scratch in middle	139.059		x		
G8	A08	Light-medium on the blue specks	137.696			x	
G9	A09	Increasing gradient of blue dots from upper LH corner to lower RH.	118.902		x		
G10	A10	Uniform surface, some wrinkles	65.707				x
G11	A11	Uniform surface	122.186				x
G12	A12	Uniform, light wrinkles, and 3 shallow surface cracks meeting near the center	106.232				x
G13	A13	Uniform, light scratches from sanding	99.531				x
G14	A14	Increasing gradient of blue dots from upper LH corner to lower RH.	134.737		x		
G15	A15	Small surface fracture across whole sample from top to bottom	118.206				x
G16	A16	Uniform surface, two lines from wax left-to-right	97.628				x
G17	A17	Uniform surface, crumb	128.093				x
G18	A18	Uniform surface, possible fine crack near the middle	98.768				x



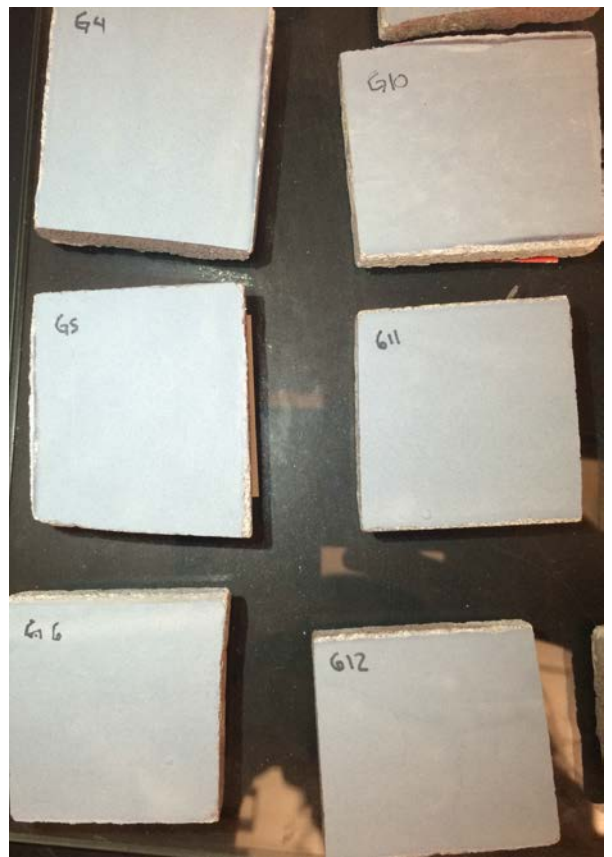
Sample		Surface Comments Pre-Test	Stress (psi)	speck heavy	speck medium	speck light	no specks
G19	A19	Uniform surface, possible fine crack near the center right edge, wax line across top	122.682				x
G20	A20	Uniform surface, light on the specks	123.614			x	
G21	A21	Large round pit, medium-heavy on the blue dots	114.558	x			
G22	A22	Uniform surface, medium specks	115.026		x		
G23	A23	Uniform surface, light on the specks	115.803			x	
G24	A24	Uniform surface, heavy on the specks	129.135	x			
G25	A25	Uniform surface, medium-heavy specks	117.700		x		
G26	A26	Uniform surface	129.531				x
G27	A27	Uniform surface, some wrinkles	132.539				x
G28	A28	Uniform surface, light-medium specks	169.575		x		
G29	A29	Uniform surface, light specks, line from wax	144.618			x	
G30	A30	Uniform surface, medium specks	107.797		x		
G31	A31	Uniform surface	102.278				x
G32	A32	Uniform surface, light on the specks	150.368			x	
G33	A33	Uniform surface, very light specks, lots of wrinkles	69.408			x	
G34	A34	Uniform surface, very light specks, small wrinkles	98.095			x	
G35	A35	Uniform surface, very light specks, lots of wrinkles	113.695			x	
G36	A36	Uniform surface, some wrinkles	91.484				x
I1	B01	Wrinkles, few pores	187.725				
I2	B02	Few wrinkles, few pores	206.428				
I3	B03	Wax line, pretty spread out pores	177.510				
I4	B04	Some wrinkles, few pores	111.778				
I5	B05	A couple scratches from sanding, more pores along the left side	178.817				

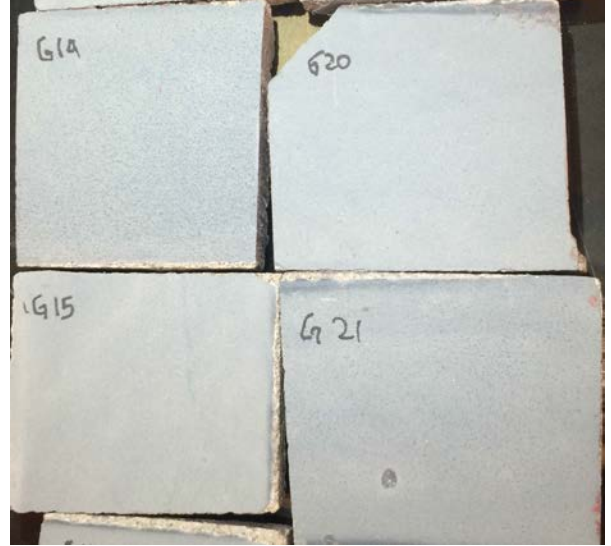


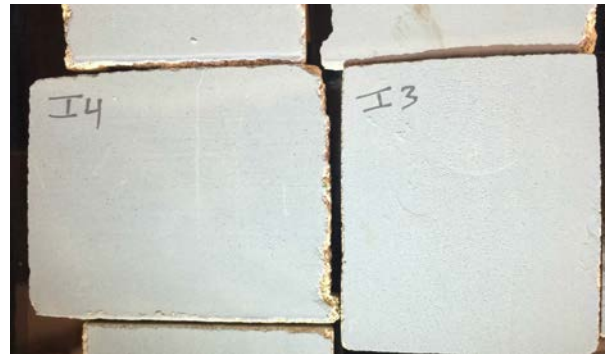
Sample		Surface Comments Pre-Test	Stress (psi)	speck heavy	speck medium	speck light	no specks
I6	B06	Wrinkles, porosity/ specks	145.820				
I7	B07	Some wrinkles, porosity gradient increasing left-to-right	204.573				
I8	B08	Porosity gradient decreasing left-to-right	185.878				
I9	B09	Lots of porosity, wax line top-to-bottom	209.769				
I10	B10	Regular ridged wrinkles, pretty even porosity along the middle, wax line	144.830				
I11	B11	Lots of wrinkles, wax line, some porosity	212.521				
I12	B12	Wrinkles, wax line, little porosity	187.440				
H1	C01	Light specks, small wrinkles	90.229				x
H2	C02	Die lines from wax, some oriented wrinkles, crack across corner	144.270				x
H3	C03	Heavy on specks, big divot on bottom center	184.931	x			
H4	C04	Some wrinkles, crack down right edge	153.844				x
H5	C05	Wrinkles, low on specks	173.247			x	
H6	C06	light specks, crack across middle-top	117.521			x	
H7	C07	Medium specks, otherwise uniform	174.273		x		
H8	C08	Crack down left- center, otherwise uniform	135.605				x
H9	C09	Medium specks, otherwise uniform	198.463		x		
H10	C10	Medium-light specks	102.483		x		
H11	C11	Medium-heavy specks, divot away from center, otherwise uniform	123.241		x		
H12	C12	Uniform, crack across center	119.096				x
H13	C13	Wrinkles, no specks	125.857				x
H14	C14	Medium-heavy specks, crack from bottom center up	193.686	x			
H15	C15	Cracks headed into center from side, not in center. Otherwise pretty uniform	175.631				x



Sample		Surface Comments Pre-Test	Stress (psi)	speck heavy	speck medium	speck light	no specks
H16	C16	Medium specks, otherwise uniform	120.534		x		
H17	C17	Light specks, uniform	117.899			x	
H18	C18	Medium-light specks	174.486			x	
H19	C19	Pretty uniform	121.825				x
H20	C20	Wrinkles, wax line, medium specks	100.058		x		
H21	C21	Wax line, down left, crack up right, wrinkles	130.268				x
H22	C22	Pretty uniform except for a crack up the center to the middle	129.106				x
H23	C23	Uniform, heavy specks	125.543	x			
H24	C24	Very wrinkled, wax lines, no specks	142.017				x
H25	C25	Medium specks, otherwise uniform	208.974		x		
H26	C26	Wrinkled, no specks, crack down left side	144.091				x
H27	C27	Wrinkles, no specks	138.983				x
H28	C28	Medium specks, some wrinkles	93.570		x		
H29	C29	Wrinkles, crack right through the middle	166.263				x
H30	C30	Speck gradient increasing from light on the left to heavy on the right	137.864		x		
H31	C31	Wax line, light specks	169.182			x	
H32	C32	Line, little wrinkles, low specks	155.174			x	
H33	C33	Crack from top left to center right, few specks	162.248			x	
H34	C34	Light specks, otherwise uniform	123.619			x	
H35	C35	Medium-light specks	95.677			x	







Appendix B: Button Surfaces After Testing

Rather than writing down visual descriptions of the sample left on each button after testing, we photographed each one. The buttons were held in the gluing fixture, which worked well to hold them at a repeatable height and angle. Table BI shows most of the buttons from the preliminary tests in chronological order. These images were taken with a phone camera. During the final tests, we found that with careful alignment and a quick finger on the shutter, we could take higher resolution images by holding the phone up to the stereoscope's left lens. The phone has to be 1-2 inches away from the eyepiece to see the whole image. It takes a steady hand to hold it in one place long enough to get the picture, since a slight wobble moves the camera out of the light coming through the eyepiece. Table BII shows the final test buttons. Failures in Group C were both shallow and rounded, unlike Groups A and B, which were mostly flat.

Table VIII. Button surfaces B-D from preliminary tests. All samples are standard green shells


















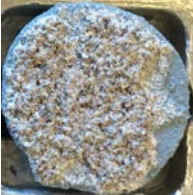


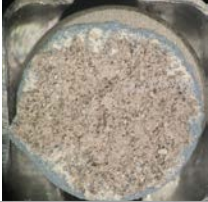





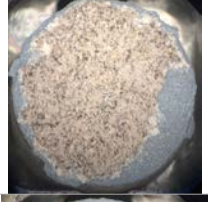
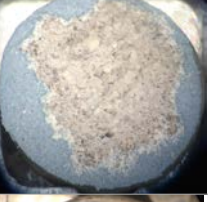


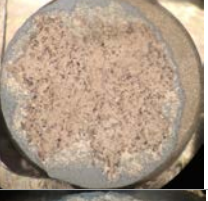



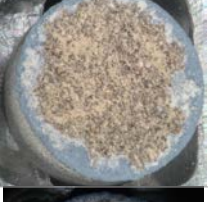


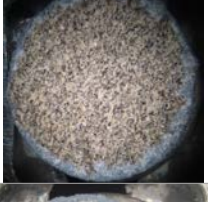




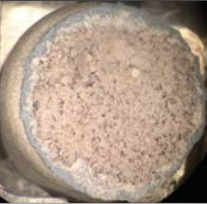





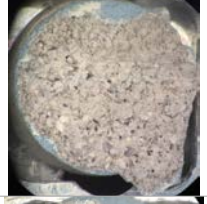

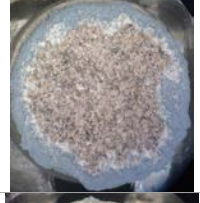


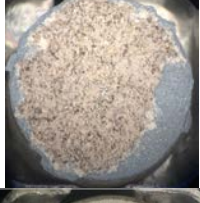
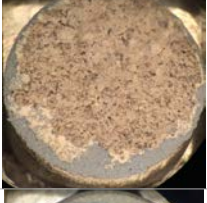



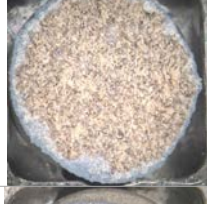
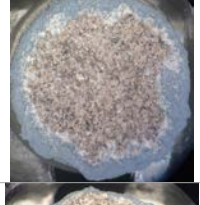





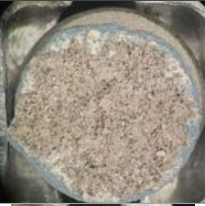



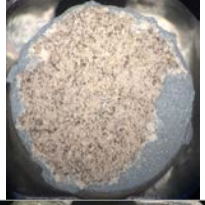




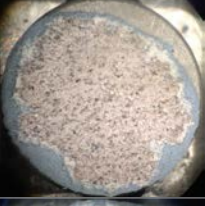

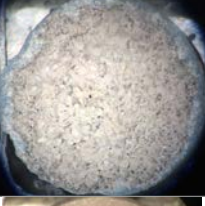
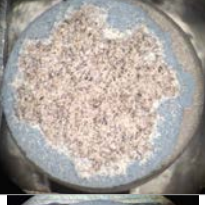



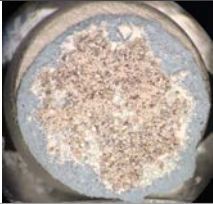



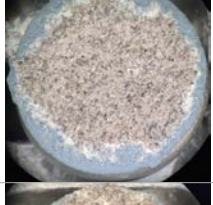
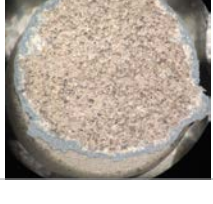
Sample	Button	Button	Button	Button			
B1		C1		D1		D6	
B2		C2		D2		D7	
B3		C3		D3		D8	
B4		C4		D4		D9	
B5		C5		D5		D10	

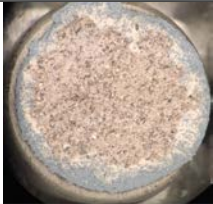
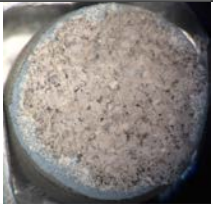



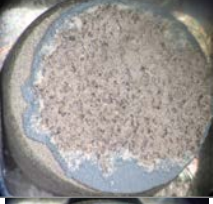

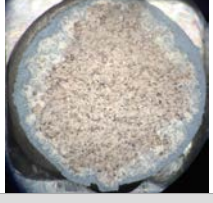

Table IX. Button Surfaces A-C from final tests

Standard, green		Add'l secondary coat, green.		Standard, fired	
A01		C01		B01	
A02		C02		B02	
A03		C03		B03	
A04		C04		B04	
A05		C05		B05	
A06		C06		B06	
A07		C07		B07	

Standard, green		Add'l secondary coat, green.		Standard, fired	
A08		C08		B08	
A09		C09		B09	
A10		C10		B10	
A11		C11		B11	
A12		C12		B12	
A13		C13		B13 (from first test)	
A14		C14		B14 (from first test)	
A15		C15		B15 (from first test)	

Standard, green		Add'l secondary coat, green.		Standard, fired	
A16		C16			
A17		C17			
A18		C18			
A19		C19			
A20		C20			
A21		C21			
A22		C22			
A23		C23			

Standard, green		Add'l secondary coat, green.		Standard, fired	
A24		C24			
A25		C25			
A26		C26			
A27		C27			
A28		C28			
A29		C29			
A30		C30			
A31		C31			

Standard, green		Add'l secondary coat, green.		Standard, fired	
A32		C32			
A33		C33			
A34		C34			
A35		C35			
A36					

Appendix C: Depth Results and Statistics

The following graphs (Fig. 53-55) show the failure stresses arranged by failure mode for each sample group.

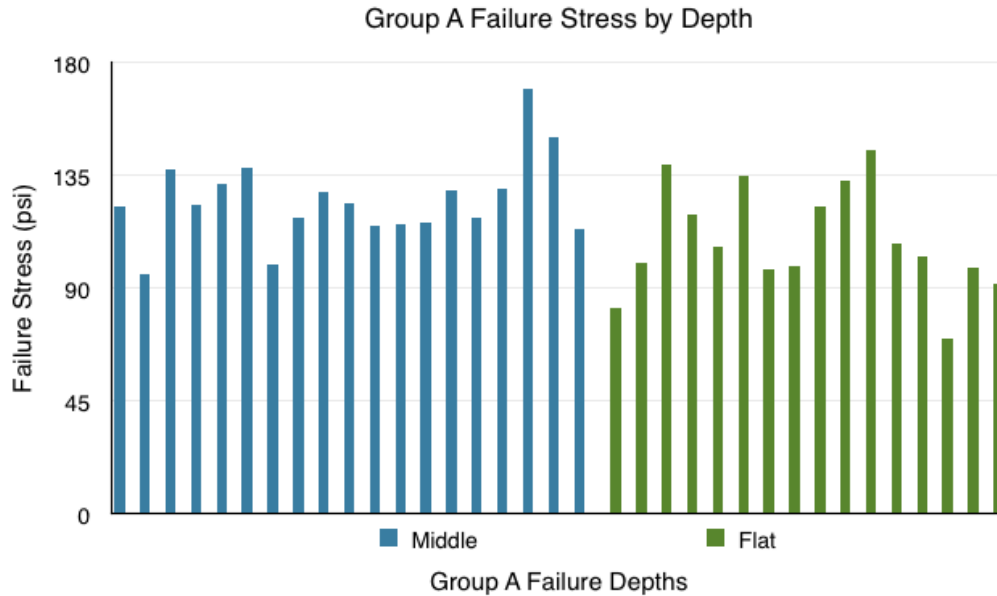


Figure 53. Flat and middle failure stresses in Group A. The flat failures in Group A were in the same range as the middle failures, with the exception of two weaker flat samples, and one stronger middle sample that stood out between data sets.

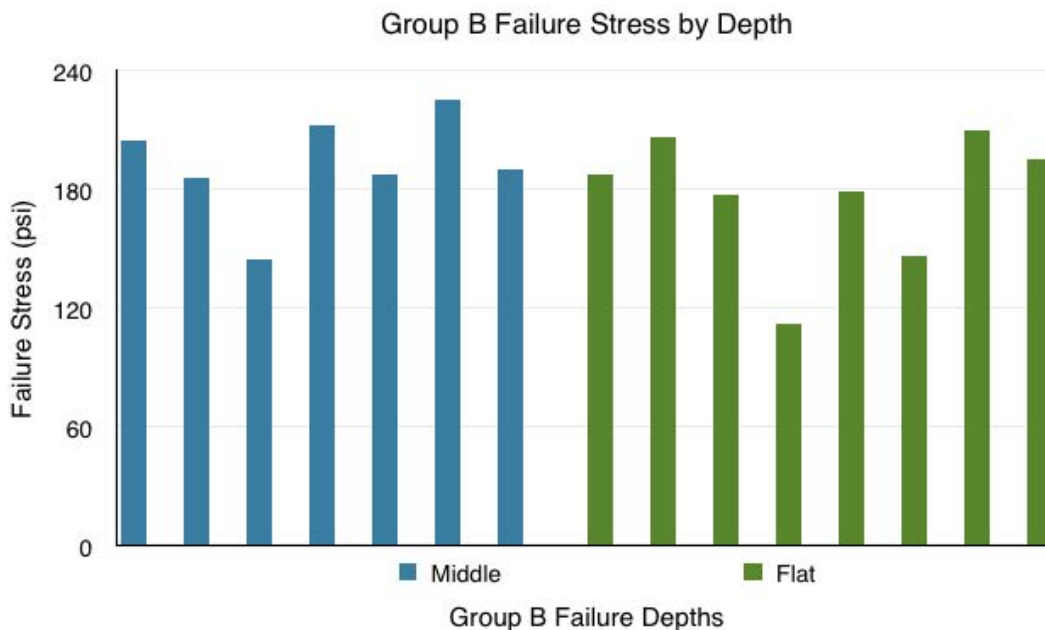
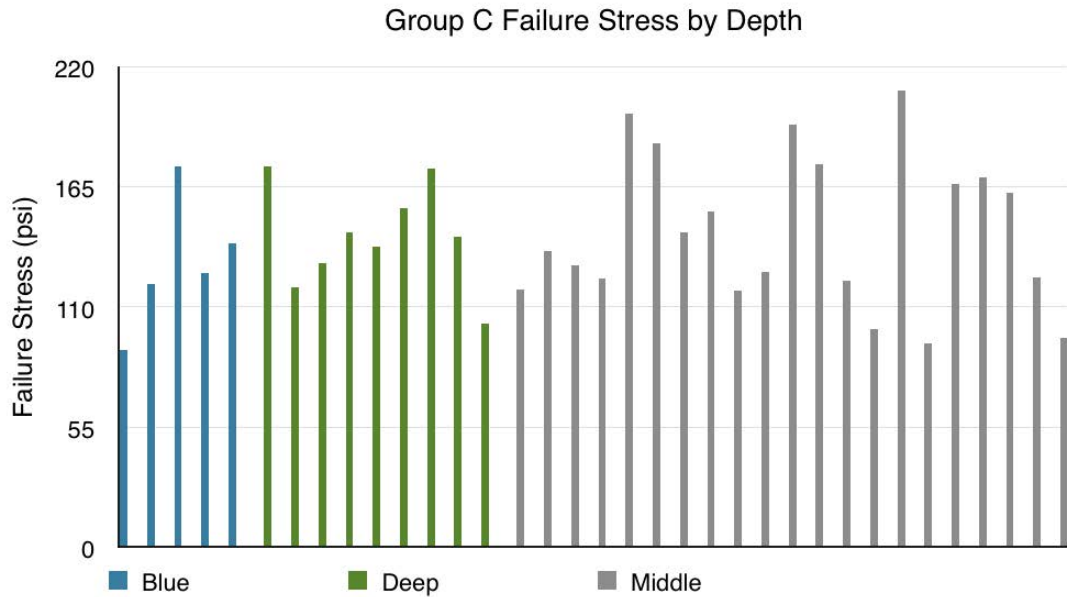


Figure 54. Flat and middle failure stresses in Group B. Like Group A, Group B's failure stresses were mostly in the same range, regardless of failure depth. The middle failures had one exceptionally strong sample, and the flat failures had one weak sample.



Group C Failure Depths

Figure 55. Blue, deep, and middle failure stresses in Group C. With the larger number of sample across the three failure depths, the only data points that stand out are four stronger middle failures. However, there is no observable general trend.

Figure 56 shows a test for equal variance, using “Group with Depth” labels represent the sample group, and the failure mode (Flat, Middle, Blue, Deep). These tests were run before we re-labeled the groups as follows: G=A, I=B, and H=C

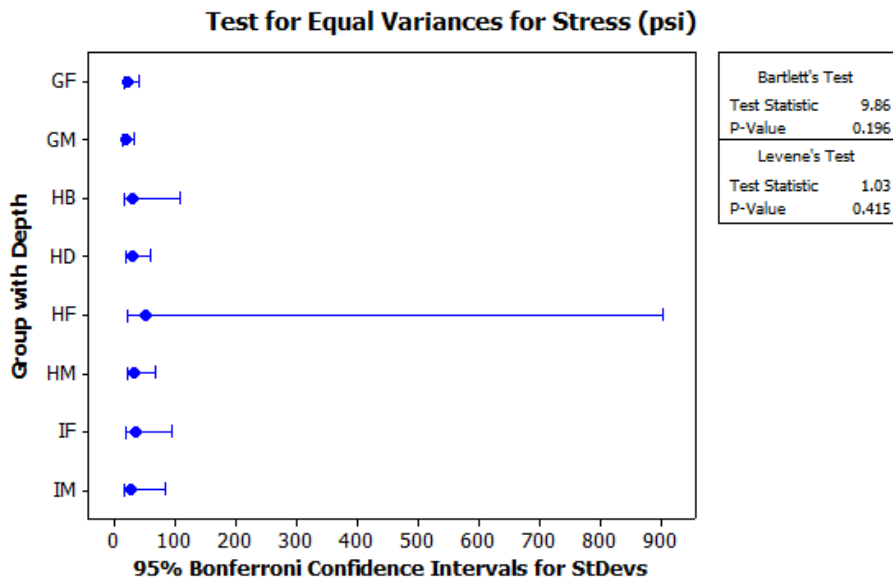


Figure 56. Test for equal variances in Groups A-C. A test for comparing the standard deviations of the different failure groupings.

The test for normality of the standardized residuals (Fig. 57) from the depth tests showed that a normal distribution approximates them well.

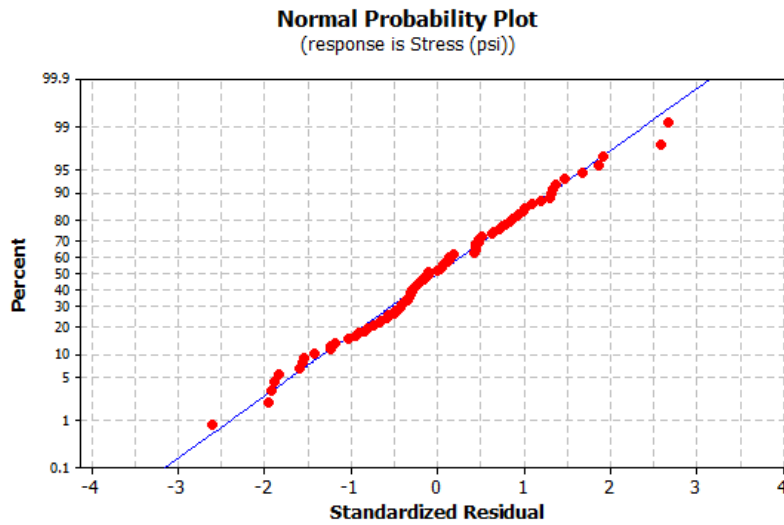


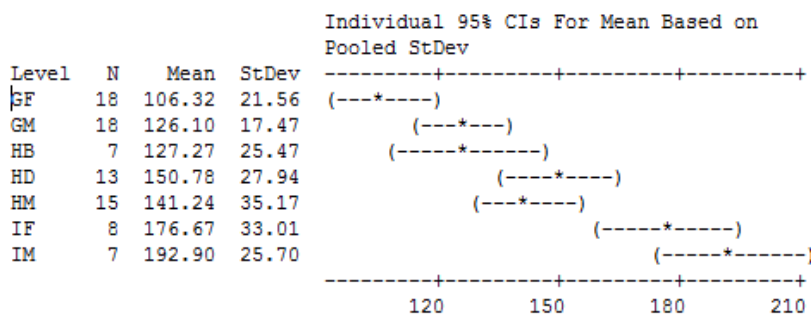
Figure 57. Normality test for standardized residuals of stresses by failure mode. The normal distribution is an appropriate model to analyze this data, because the standardized residuals mostly fit the normal curve line.

Finally, the Minitab printouts from the ANOVA analysis follow.

One-way ANOVA: Stress (psi) versus Group with Depth

Source	DF	SS	MS	F	P
Group with Depth	6	56732	9455	13.52	0.000
Error	79	55258	699		
Total	85	111989			

S = 26.45 R-Sq = 50.66% R-Sq(adj) = 46.91%



Pooled StDev = 26.45

Grouping Information Using Tukey Method

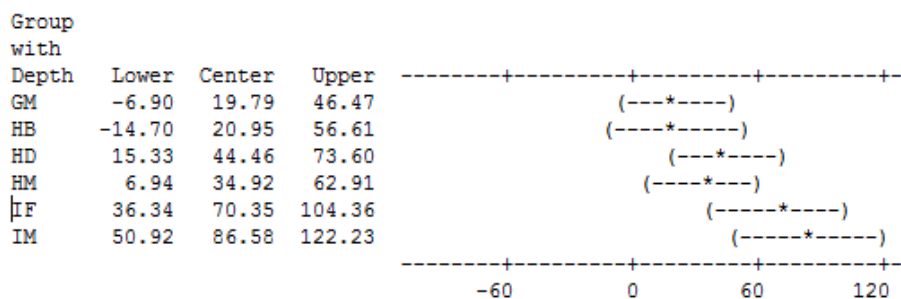
Group with Depth	N	Mean	Grouping
IM	7	192.90	A
IF	8	176.67	A B
HD	13	150.78	B C
HM	15	141.24	C
HB	7	127.27	C D
GM	18	126.10	C D
GF	18	106.32	D

Means that do not share a letter are significantly different.

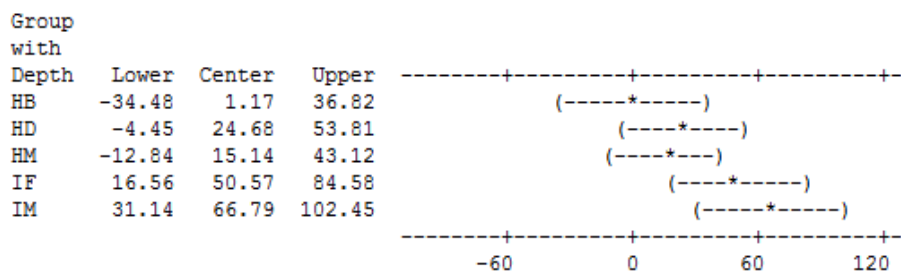
Tukey 95% Simultaneous Confidence Intervals
 All Pairwise Comparisons among Levels of Group with Depth

Individual confidence level = 99.67%

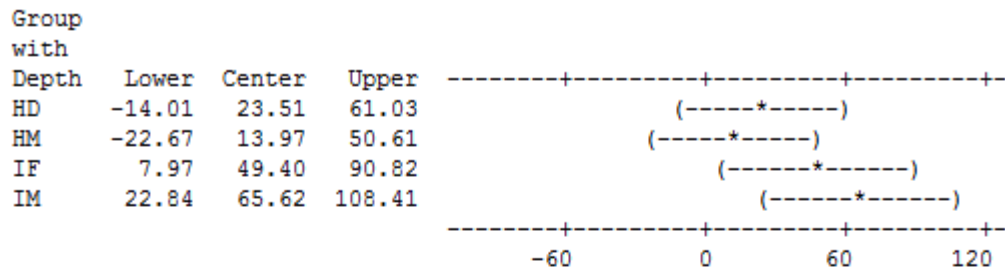
Group with Depth = GF subtracted from:



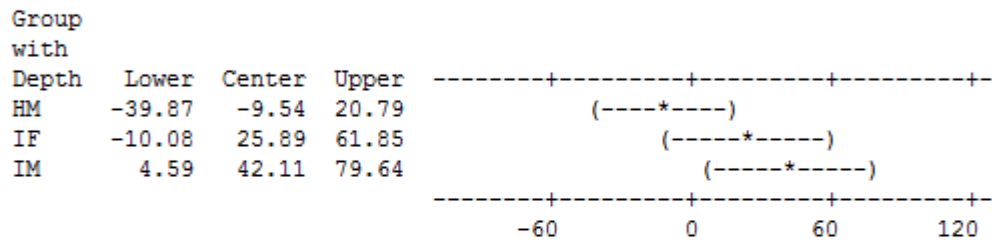
Group with Depth = GM subtracted from:



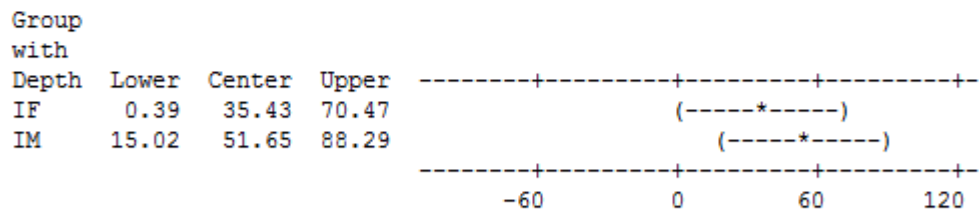
Group with Depth = HB subtracted from:



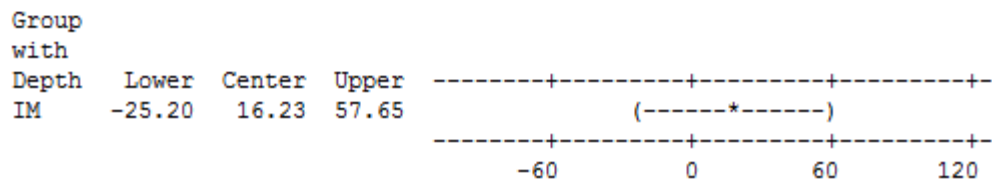
Group with Depth = HD subtracted from:



Group with Depth = HM subtracted from:



Group with Depth = IF subtracted from:



Appendix D: Surface Specks Graph

The graph in Figure 58 showed that the surface specks do not seem to generate a trend in sample strength.

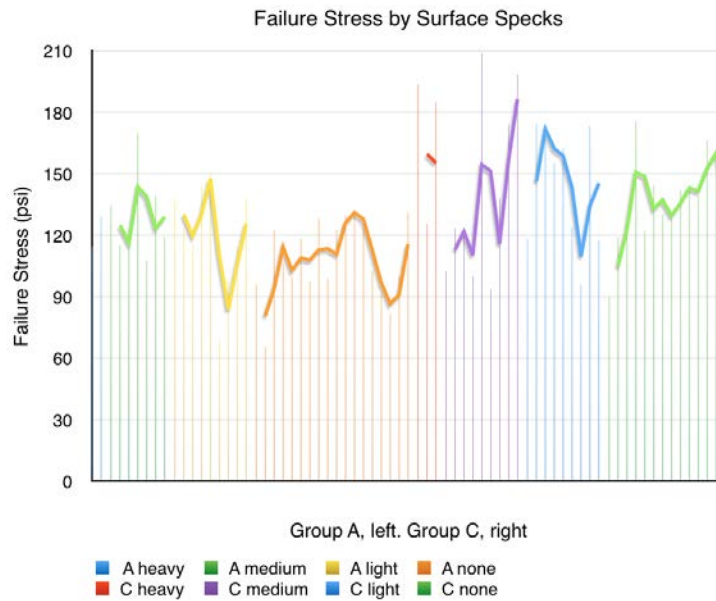


Figure 58. Failure stresses by amount of specks on each sample's surface. While the moving average trendline seems to show a slight strength increase for samples with more specks, the data ranges do not show an actual trend.

Appendix E: Statistical Analysis of Groups

The following graphs and Minitab printouts show the supporting statistics for testing differences in group means. Figure 59 shows that the data can be analyzed as normal.

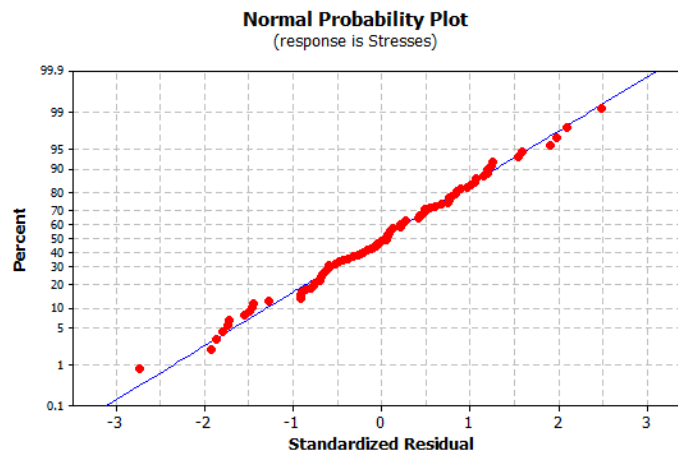


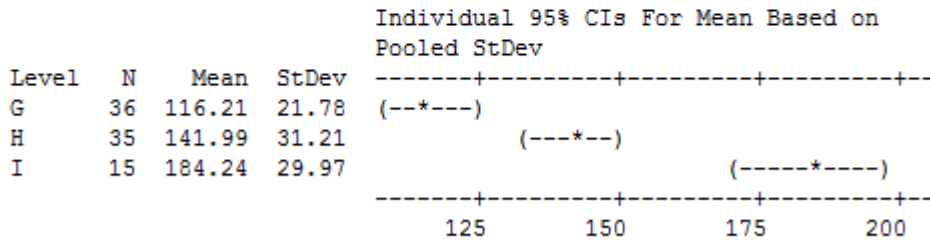
Figure 59. A normality plot of the ANOVA residuals for the groups, showing that they all fit within ± 3 standard deviations of the mean. According to this graph, a normal distribution is an acceptable analysis model for this data.

The last several images show the Minitab printouts from the ANOVA for this analysis.

One-way ANOVA: Stresses versus Groups

Source	DF	SS	MS	F	P
Groups	2	49696	24848	33.11	0.000
Error	83	62294	751		
Total	85	111989			

S = 27.40 R-Sq = 44.38% R-Sq(adj) = 43.04%



Pooled StDev = 27.40

Grouping Information Using Tukey Method

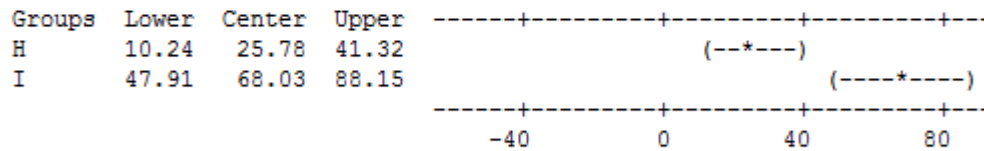
Groups	N	Mean	Grouping
I	15	184.24	A
H	35	141.99	B
G	36	116.21	C

Means that do not share a letter are significantly different.

Tukey 95% Simultaneous Confidence Intervals
All Pairwise Comparisons among Levels of Groups

Individual confidence level = 98.09%

Groups = G subtracted from:



Groups = H subtracted from:

